PHANGS–JWST First Results: Rapid Evolution of Star Formation in the Central Molecular Gas Ring of NGC 1365

Eva Schinnerer[1] , Eric Emsellem[2,3] , Jonathan D. Henshaw[1,4] , Daizhong Liu[5] , Sharon E. Meidt[6] , Miguel Querejeta[7] , Florent Renaud[8] , Mattia C. Sormani[9] , Jiayi Sun[10,11] , Oleg V. Egorov[12] , Kirsten L. Larson[13] , Adam K. Leroy[14] , Erik Rosolowsky[15] , Karin M. Sandstrom[16] , T. G. Williams[1] , Ashley. T. Barnes[17] , F. Bigiel[17] , Mélanie Chevance[9,18] , Yixian Cao[5] , Rupali Chandar[19] , Daniel A. Dale[20] , Cosima Eibensteiner[17] , Simon C. O. Glover[9] , Kathryn Grasha[21,22] , Stephen Hannon[23], Hamid Hassani[15] , Jaeyeon Kim[9] , Ralf S. Klessen[9,24] , J. M. Diederik Kruijssen[18] , Eric J. Murphy[25] , Justus Neumann[1] , Hsi-An Pan[26] , Jérôme Pety[27,28] , Toshiki Saito[29] , Sophia K. Stuber[1] , Robin G. Treß[30] , Antonio Usero[7] , Elizabeth J. Watkins[31] , and Bradley C. Whitmore[32]

(PHANGS)

[1] Max Planck Institute for Astronomy, Königstuhl 17, D-69117, Germany; schinner@mpia.de
[2] European Southern Observatory, Karl-Schwarzschild-Straße 2, D-85748 Garching, Germany
[3] Univ Lyon, Univ Lyon1, ENS de Lyon, CNRS, Centre de Recherche Astrophysique de Lyon UMR5574, F-69230 Saint-Genis-Laval, France
[4] Astrophysics Research Institute, Liverpool John Moores University, 146 Brownlow Hill, Liverpool L3 5RF, UK
[5] Max-Planck-Institut für Extraterrestrische Physik (MPE), Giessenbachstr. 1, D-85748 Garching, Germany
[6] Sterrenkundig Observatorium, Universiteit Gent, Krijgslaan 281 S9, B-9000 Gent, Belgium
[7] Observatorio Astronómico Nacional (IGN), C/Alfonso XII, 3, E-28014 Madrid, Spain
[8] Department of Astronomy and Theoretical Physics, Lund Observatory, Box 43, SE-221 00 Lund, Sweden
[9] Universität Heidelberg, Zentrum für Astronomie, Institut für Theoretische Astrophysik, Albert-Ueberle-Straße 2, D-69120 Heidelberg, Germany
[10] Department of Physics and Astronomy, McMaster University, 1280 Main Street West, Hamilton, ON L8S 4M1, Canada
[11] Canadian Institute for Theoretical Astrophysics (CITA), University of Toronto, 60 St George Street, Toronto, ON M5S 3H8, Canada
[12] Astronomisches Rechen-Institut, Zentrum für Astronomie der Universität Heidelberg, Mönchhofstraße 12-14, D-69120 Heidelberg, Germany
[13] AURA for the European Space Agency (ESA), Space Telescope Science Institute, 3700 San Martin Drive, Baltimore, MD 21218, USA
[14] Department of Astronomy, The Ohio State University, 140 West 18th Avenue, Columbus, OH 43210, USA
[15] Department of Physics, University of Alberta, Edmonton, Alberta, T6G 2E1, Canada
[16] Center for Astrophysics & Space Sciences, University of California, San Diego, 9500 Gilman Drive, San Diego, CA 92093, USA
[17] Argelander-Institut für Astronomie, Universität Bonn, Auf dem Hügel 71, D-53121, Bonn, Germany
[18] Cosmic Origins Of Life (COOL) Research DAO[35]
[19] Ritter Astrophysical Research Center, University of Toledo, Toledo, OH 43606, USA
[20] Department of Physics and Astronomy, University of Wyoming, Laramie, WY 82071, USA
[21] Research School of Astronomy and Astrophysics, Australian National University, Canberra, ACT 2611, Australia
[22] ARC Centre of Excellence for All Sky Astrophysics in 3 Dimensions (ASTRO 3D), Australia
[23] Department of Physics and Astronomy, University of California, Riverside, CA 92521, USA
[24] Universität Heidelberg, Interdisziplinäres Zentrum für Wissenschaftliches Rechnen, Im Neuenheimer Feld 205, D-69120 Heidelberg, Germany
[25] National Radio Astronomy Observatory, 520 Edgemont Road, Charlottesville, VA 22903, USA
[26] Department of Physics, Tamkang University, No. 151, Yingzhuan Road, Tamsui District, New Taipei City 251301, Taiwan
[27] IRAM, 300 rue de la Piscine, F-38400 Saint Martin d'Hères, France
[28] LERMA, Observatoire de Paris, PSL Research University, CNRS, Sorbonne Universités, 75014 Paris, France
[29] National Astronomical Observatory of Japan, 2-21-1 Osawa, Mitaka, Tokyo, 181-8588, Japan
[30] Institute of Physics, Laboratory for Galaxy Evolution and Spectral Modelling, EPFL, Observatoire de Sauverny, Chemin Pegais 51, 1290 Versoix, Switzerland
[31] Astronomisches Rechen-Institut, Zentrum für Astronomie der Universität Heidelberg, Mönchhofstraße 12-14, D-69120 Heidelberg, Germany
[32] Space Telescope Science Institute, 3700 San Martin Drive, Baltimore, MD 21218, USA

Abstract

Large-scale bars can fuel galaxy centers with molecular gas, often leading to the development of dense ringlike structures where intense star formation occurs, forming a very different environment compared to galactic disks. We pair $\sim0\rlap{.}''3$ (30 pc) resolution new JWST/MIRI imaging with archival ALMA CO(2–1) mapping of the central ~5 kpc of the nearby barred spiral galaxy NGC 1365 to investigate the physical mechanisms responsible for this extreme star formation. The molecular gas morphology is resolved into two well-known bright bar lanes that surround a smooth dynamically cold gas disk ($R_{\rm gal} \sim 475$ pc) reminiscent of non-star-forming disks in early-type galaxies and likely fed by gas inflow triggered by stellar feedback in the lanes. The lanes host a large number of JWST-identified massive young star clusters. We find some evidence for temporal star formation evolution along the ring. The complex kinematics in the gas lanes reveal strong streaming motions and may be consistent with convergence of gas streamlines expected there. Indeed, the extreme line widths are found to be the result of inter-"cloud" motion between gas peaks; SCOUSEPY decomposition reveals multiple components with line widths of $\langle \sigma_{\rm CO,scouse} \rangle \approx 19\,{\rm km\,s^{-1}}$ and surface densities of $\langle \Sigma_{\rm H_2,scouse} \rangle \approx 800\,M_\odot\,{\rm pc^{-2}}$, similar to the properties

observed throughout the rest of the central molecular gas structure. Tailored hydrodynamical simulations exhibit many of the observed properties and imply that the observed structures are transient and highly time-variable. From our study of NGC 1365, we conclude that it is predominantly the high gas inflow triggered by the bar that is setting the star formation in its CMZ.

Unified Astronomy Thesaurus concepts: Barred spiral galaxies (136); Starburst galaxies (1570); Star formation (1569); Interstellar medium (847)

1. Introduction

Galaxy centers are special places for star formation to occur. They can contribute 10%–100% of the overall star formation in galaxies (Kormendy & Kennicutt 2004), capture extreme conditions, and represent major sites of feedback to the circumgalactic medium (e.g., Veilleux et al. 2020). It is expected that star formation in galaxy centers proceeds differently than in disks. The dynamical time in galaxy centers is short (1–50 Myr), with gas inflows driven by stellar bars (and spirals), large-scale gas outflows launched by active galactic nuclei (AGN) and central starbursts, and intense radiation fields due to the high stellar densities (and AGN, when present). All of these phenomena affect the balance between the self-gravity of the molecular gas and factors (e.g., turbulence, shear, magnetic fields, tidal forces, and cosmic-ray flux) that support the gas against gravitational collapse (e.g., Chevance et al. 2020; Girichidis et al. 2020). The closest galaxy centers allow for high physical resolution studies to assess the impact of these environmental factors, making them unique targets for testing star formation theories (for recent examples utilizing observations of molecular gas, see, e.g., Callanan et al. 2021; Levy et al. 2021; Martín et al. 2021; Behrens et al. 2022; Eibensteiner et al. 2022).

The cold gas and dust distribution of the central regions of barred galaxies is shaped by the orbital structure of the underlying barred gravitational potential and typically forms two bar lanes along the leading sides of the bar that generally curve at smaller galactocentric radii (right panels of Figure 1; see seminal paper by Athanassoula 1992). In gas-rich galaxies, these inner regions (indicated as FoV in Figure 1) often host star-forming rings or spiral structures that are also referred to as nuclear rings/disks or, more generally, in analogy to the center in the Milky Way, as central molecular zones (CMZs; e.g., Morris & Serabyn 1996; Sakamoto et al. 1999; Sheth et al. 2002; Sormani et al. 2015; Martín et al. 2021; Henshaw et al. 2022).

While these rings are often sites of intense star formation (Knapen et al. 2000; Comeron et al. 2014), the physical processes leading to this massive star formation are far from understood, with several models being proposed, from gravitational instabilities in the ring (e.g., Elmegreen 1994) or in dense spurs along the straight bar lanes (Sheth et al. 2005) to gas collapse triggered at the location where gas from the lanes enters the ring (Boker et al. 2008). In past years, several simulations have started to shed more light on the mechanisms leading to these rings. Some studies report a relation between gas mass inflow rate and the resulting star formation rate (SFR) in the ring (Seo & Kim 2013; Seo et al. 2019; Sormani et al. 2020; Moon et al. 2021). A varying inflow rate has been measured for the Galactic CMZ (Sormani & Barnes 2019) and is also seen in simulations (e.g., Seo et al. 2019; Tress et al. 2020). Alternatively, quasiperiodic variations in the star formation activity are explained by the evolution of gas piling up in the ring (quiescent phase) and

becoming gravitationally unstable (starburst phase; e.g., Loose et al. 1982; Krugel & Tutukov 1993; Stark et al. 2004; Kruijssen et al. 2014; Emsellem et al. 2015; Krumholz et al. 2017; Armillotta et al. 2019).

With global simulations of gas flow in galactic centers now reaching parsec or even subparsec resolutions (e.g., Renaud et al. 2013; Tress et al. 2020), it is evident that comparisons to observations resolving similar spatial scales for the molecular gas and star formation are required to make progress in our understanding. Thanks to the advent of the Atacama Large Millimeter/submillimeter Array (ALMA) and JWST, it is now possible to probe the properties of molecular gas and (embedded) star formation at $\sim0\rlap{.}''2$, which translates to 19 pc at the distance of NGC 1365 (19.6 Mpc; Anand et al. 2021a, 2021b). In the Physics at High Angular resolution in Nearby GalaxieS[34] (PHANGS) sample, NGC 1365 is the one barred galaxy that has already received JWST observations (via PHANGS–JWST; Lee et al. 2023, this Issue) and has high-quality, high-resolution observations in the ALMA archive. Through the PHANGS set of surveys (Leroy et al. 2021a; Emsellem et al. 2022; Lee et al. 2022), abundant complementary information on this galaxy is available (e.g., Sun et al. 2022).

The nearby ($D = 19.6$ Mpc, $1'' \approx 95$ pc; Anand et al. 2021a, 2021b) barred spiral galaxy NGC 1365 hosts an AGN (Morganti et al. 1999) and has the highest SFR in the PHANGS–ALMA sample (Leroy et al. 2021a). Lindblad (1999) provided a detailed review of NGC 1365, and we summarize its basic parameters in Table 1. Located in the Fornax cluster (Jones & Jones 1980), this grand-design spiral galaxy is morphologically classified as (R')SB(r̲s,nr)bc, indicating the presence of an outer pseudoring, a weak inner pseudoring corresponding to the surroundings of the bar, and a prominent circumnuclear ring (Buta et al. 2015). The bar is remarkably long, with a full length of 17.2 kpc in the plane of the sky (Herrera-Endoqui et al. 2015), which corresponds to a deprojected value of ~28 kpc in the plane of the galaxy.[35] The nucleus harbors a number of compact radio sources and a large number of super star clusters, with star formation taking place mostly in an elongated circumnuclear ring (e.g., Kristen et al. 1997; Forbes & Norris 1998; Stevens et al. 1999; Galliano et al. 2005; Alonso-Herrero et al. 2012; Fazeli et al. 2019), which likely corresponds to the inner Lindblad resonance at $r \approx 1$ kpc reported by Lindblad et al. (1996). This ring is very rich in molecular gas (Sandqvist et al. 1995; Sakamoto et al. 2007; Gao et al. 2021; Egusa et al. 2022). The AGN is known to drive a biconical outflow seen in ionized gas (e.g., Storchi-Bergmann & Bonatto 1991; Veilleux et al. 2003; Venturi et al. 2018). All of these properties make NGC 1365 an ideal target for a detailed study of the CMZ properties utilizing ALMA and JWST observations.

---

[34] www.phangs.org
[35] This deprojection relies on the kinematic parameters from Table 1 and follows a simple deprojection considering a "1D" bar (e.g., Martin 1995).
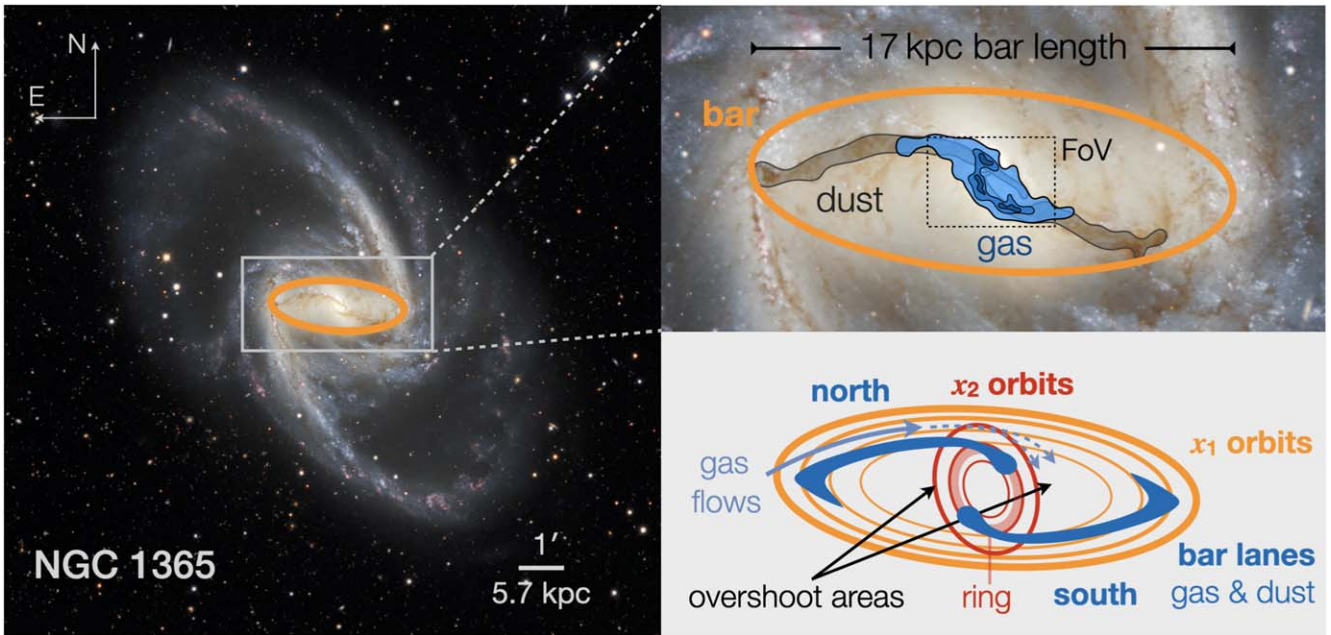
Figure 1. Inner 5 kpc in the context of the large-scale stellar bar in NGC 1365. The optical color image from DES[36] shows the 17 kpc long stellar bar (outlined by the orange ellipse as determined by Herrera-Endoqui et al. 2015) surrounded by spiral arms (left). In the zoom-in (marked as a gray box in the left panel), the bar lanes along the leading sides of the bar are highlighted via prominent extinction tracing dust (dark gray shaded) and the molecular gas distribution (blue shaded; top right). The field of view (FoV) under study in this work is shown as a dashed black box. The sketch (bottom right) outlines the basic structure of the orbits supporting the stellar bar (x_1: elongated along the bar major axis, in orange; x_2: elongated along the bar minor axis, in red) and the resulting bar lane morphology plus the inner star-forming ring. We further indicate the expected net gas flow and some relevant regions discussed in this work.

This letter is organized as follows. After a brief description of the data and simulations used (Section 2), we present the inferred properties of the gas and star formation in the starburst ring (Section 3) and discuss them in the context of the simulations in Section 4. We present our conclusions toward improving our understanding of CMZs in Section 5 before summarizing our findings (Section 6).

2. Data

With an SFR of $5\,M_\odot\,\mathrm{yr}^{-1}$, the massive starburst in the center of the strongly barred galaxy NGC 1365 makes it a prime candidate for the study of how star formation proceeds in "circumnuclear rings" or CMZs. For this, we combine archival ALMA imaging (Section 2.1) with new JWST/MIRI imaging sensitive to the embedded phase of star formation (Section 2.2) at a matched resolution of $\sim0\farcs3$ and compare to spectroscopic Hα imaging at lower resolution (Section 2.3). Here we also briefly describe the setup of the simulations (Section 2.4) used for comparison.

2.1. ALMA Data

The molecular gas distribution in the central $225'' \times 125''$ (PA $\sim -5°$) of NGC 1365 has been observed in its CO(2−1) line using the ALMA 12 m together with the ACA (7 m array and total power antennas) as part of project 2013.1.01161.S (PI: K. Sakamoto) in Cycle 2. Leroy et al. (2021a) presented the calibration and reduction for the combined data from the two more compact 12 m array configurations (C34-1 and C34-3) and the ACA. The observations with the extended 12 m configuration (C34-5) only cover the central $80'' \times 50''$ (PA $\sim -30°$), which corresponds to roughly $7.6 \times 4.8\,\mathrm{kpc}^2$. We

---

Table 1
Parameters for NGC 1365

Parameter	Value	Reference
R.A. (J2000)	$03^{\mathrm{h}}33^{\mathrm{m}}36\fs37$	(1)
Decl. (J2000)	$-36^{\mathrm{d}}08^{\mathrm{m}}25\fs4$	(1)
v_{sys} (LSR)	$1613 \pm 5\,\mathrm{km\,s^{-1}}$	(2)
D	$19.6 \pm 0.8\,\mathrm{Mpc}$	(3), (4)
Incl.	$55\fdg4 \pm 6\fdg0$	(2)
PA	$201\fdg1 \pm 7\fdg5$	(2)
$M_\star$	$\log(M_\star/M_\odot) = 11.0 \pm 0.2$	(1)
SFR	$\log(\mathrm{SFR}/M_\odot\,\mathrm{yr}^{-1}) = 1.24 \pm 0.2$	(1)
$M_{\mathrm{H_2}}$	$\log(M_{\mathrm{H_2}}/M_\odot) = 10.3$	(1)[a]
$\mathrm{SFR_{starburst}}$	$\log(\mathrm{SFR}/M_\odot\,\mathrm{yr}^{-1}) \approx 0.7$	(5)[b]
$M_{\mathrm{H_2,starburst}}$	$\log(M_{\mathrm{H_2}}/M_\odot) \approx 10.0$	(1)[c]
Bar PA	$86°$	(6)
Bar radius[d]	$90\farcs4$ (8.6 kpc)	(6)

Notes. The parameters are taken from (1) Leroy et al. (2021a), (2) Lang et al. (2020), (3) Anand et al. (2021a), (4) Anand et al. (2021b), (5) Belfiore et al. (2022), and (6) Herrera-Endoqui et al. (2015).
[a] H$_2$ gas mass assuming a standard conversion factor and $R_{21} = 1$ (see Section 2.1) including aperture correction.
[b] SFR of the starburst (i.e., inside $R_{\mathrm{gal}} \leqslant 1.8$ kpc) as measured on the attenuation-corrected Hα map from PHANGS–MUSE (Emsellem et al. 2022).
[c] H$_2$ gas mass of the starburst (i.e., inside $R_{\mathrm{gal}} \leqslant 1.8$ kpc).
[d] Projected radius (Herrera-Endoqui et al. 2015); the deprojected bar radius is ~14 kpc using the orientation provided in the table.

applied the observatory-delivered calibration (*scriptForPI.py*). The PHANGS–ALMA imaging pipeline (Leroy et al. 2021b) was adapted and used to simultaneously image the three 12 m array configurations together with the 7 m array data. In a next step, the total power data were feathered with the interferometric data cube as outlined in Leroy et al. (2021b). The resulting cube has a spectral resolution of about 2.54 km s^{-1};

---

an angular resolution of $\sim 0\rlap{.}{''}31$, which corresponds to ~ 30 pc at our adopted distance of 19.57 ± 0.78 Mpc (Anand et al. 2021a, 2021b); and an rms of 0.72 K.

The resulting data products are derived with the PHANGS–ALMA imaging pipeline as described by Leroy et al. (2021b). For the analysis, we utilize the following products: an integrated intensity map using the broad mask (i.e., high completeness), a velocity field derived with a prior, a peak temperature map obtained in 12.5 km s^{-1} wide channels, and a map of the effective velocity width. Differences between our integrated CO(2−1) intensity map and that presented by Alonso-Herrero et al. (2020) are due to the fact that the latter was derived from the extended 12 m array configuration data only.

In order to convert CO(2−1) intensities I_{CO21} to H_2 gas mass surface densities Σ_{H_2}, we adopt a Galactic conversion factor of $\alpha_{CO} = 4.35\, M_\odot\, \mathrm{pc}^{-2}(\mathrm{K\ km\ s}^{-1})^{-1}$ (Bolatto et al. 2013) and a CO(2−1)-to-CO(1−0) ratio of $R_{21} = 1$. Leroy et al. (2023a, this Issue) recommended this ratio for high mid-IR (MIR) surface brightness (e.g., $I_{21\mu m} \geqslant 10$ MJy sr^{-1} as presented here) based on an extensive comparison of CO and MIR emission in nearby galaxies. This is close to the R_{21} values around 0.8–0.9 obtained at $\sim 3''$ resolution for the region studied here (Liu et al. 2023, this Issue). Teng et al. (2022) reported a lower $\alpha_{CO} \approx 0.5-2.0\, M_\odot\, \mathrm{pc}^{-2}(K\ \mathrm{km\ s}^{-1})^{-1}$ for the starburst ring in the nearby barred galaxy NGC 3351 based on non-LTE modeling of multiple CO lines. Hence, the H_2 surface densities could be a factor of 2–4× lower than quoted here, depending on the exact conditions of the molecular interstellar medium (ISM; see also a detailed analysis of NGC 1365's central region by Liu et al. 2023).

2.2. JWST/MIRI and NIRCam Imaging

As part of the PHANGS–JWST Treasury program (project ID 2107; Lee et al. 2023, this Issue), JWST has mapped NGC 1365 using the MIRI instrument in a 2×2 mosaic in four filters (F770W, F1000W, F1130W, and F2100W) and a 2×1 mosaic using NIRCam in an additional four filters (F200W, F300M, F335M, and F360M), the most prescient for this work being the F200W image. Each of these mosaic tiles uses a four-point dither pattern to ensure good sampling of the point-spread function (PSF; $0\rlap{.}{''}066/0\rlap{.}{''}243/0\rlap{.}{''}321/0\rlap{.}{''}368/0\rlap{.}{''}665$ at F200W/F770W/F1000W/F1130W/F2100W). Full details of the data processing are given in Lee et al. (2023), but as a brief overview, we use the public JWST pipeline,[37] mostly with default settings with the latest reference files at the time of processing (early 2022 September, although we use the improved MIRI flats delivered in mid-September; K. Gordon, private communication). These latest files improve upon the mosaics that were available from the MAST archive. For the MIRI imaging, we use dedicated background observations of the galaxy to remove any thermal background from the observations, as recommended by the observatory (Rigby et al. 2022). The thermal background is negligible in the NIRCam imaging, so this step is not performed for the F200W data. We found that the simultaneously recorded data of MIRI's Lyot coronagraph has a noticeably different background from the main science detector, and we mask this out before mosaicking. Given the outstanding background uncertainties, we currently image each of the MIRI fields separately

---

[37] https://github.com/spacetelescope/jwst

and mosaic them together outside of the JWST pipeline, but we expect that the background matching may improve as the pipeline is updated. Absolute astrometric alignment is based on cross-correlation of the MIRI mosaics with an already-aligned NIRCam image taken as part of the same observations that uses asymptotic giant branch (AGB) stars in the galaxy detected in Hubble Space Telescope (HST) imaging (for details, see Lee et al. 2023). The final NIRCam F200W mosaic has a sensitivity of around 0.1 MJy sr^{-1}, and the final MIRI mosaics have sensitivities that vary from around 0.1 MJy sr^{-1} for F770W to 0.3 MJy sr^{-1} for F2100W. Finally, as our images are filled with galaxy emission, to achieve an absolute flux level, we anchor the fluxes to existing Spitzer or WISE imaging, deriving a constant offset for each band (see Appendixes A and B of Leroy et al. 2023a, this Issue). We perform no convolution to the images to maximize the resolution of each MIRI image.

2.3. PHANGS–MUSE Data Products

We make use of data from the PHANGS–MUSE survey (PI: Schinnerer; Emsellem et al. 2022), which imaged significant parts of the star-forming disk using the optical integral field unit (IFU) MUSE mounted on the VLT. Data processing and generation of ionized gas emission line maps follow standard procedures and are described in detail in Emsellem et al. (2022). We utilize the Hα emission line map from the copt (i.e., convolved to a common resolution across the spectral range and all pointings) $1\rlap{.}{''}15$ resolution mosaic with a sensitivity of 2×10^{-20} erg s^{-1} cm^{-2} spaxel^{-1} for $0\rlap{.}{''}2$ spaxels. In addition, the attenuation-corrected Hα map (assuming $R_V = 3.1$) and corresponding $E(B-V)$ map (from the Balmer decrement; assuming case B recombination, temperature $T = 10^4$ K, density $n_e = 10^2$ cm^{-3}) derived by Belfiore et al. (2022) from the PHANGS–MUSE copt data products are used.

2.4. RAMSES Hydrodynamical Simulations of NGC 1365

In the course of the PHANGS project, we designed and ran dedicated hydrodynamical simulations tuned to mock the overall properties of a subsample of PHANGS targets. We briefly present here some results from the NGC 1365–like simulation (see E. Emsellem et al. 2023, in preparation, for a more extensive description). To set up the simulations, we made use of NGC 1365's known observed global properties (see Table 1) and radial profiles, namely, the molecular and H I content, stellar mass, stellar density profile, and CO velocity profile (Sun et al. 2022), together with geometrical considerations (inclination, PA of the line of nodes), to construct a multicomponent axisymmetric three-dimensional mass and dynamical model including stars, dark matter, and gas using the multi-Gaussian expansion formalism (Emsellem et al. 1994, 2015) as in, e.g., Renaud et al. (2013). We then conducted a noncosmological adaptive mesh refinement hydrodynamical simulation using the RAMSES code (Teyssier 2002), starting with initial conditions based on a realization of that model, with live dark matter and stellar particles over a grid of 120×120 kpc^2, with a maximum sampling for the gas cells of ~ 3.7 pc (maximum refinement level of 15). We adopt subgrid prescriptions for the cooling, star formation, feedback, and stellar evolution, as in Renaud et al. (2021). In short, the simulation accounts for atomic and molecular cooling, heating from an external UV flux, and star formation at a constant efficiency per freefall time (2%) in dense gas (150 cm^{-3}), with

initial masses of new particles of $2000\,M_\odot$. It also includes prescriptions for stellar winds, radiative pressure, and Type II and Ia supernova feedback with energy released based on the resolution of the local cooling radius (Agertz & Kravtsov 2015; Agertz et al. 2021). The NGC 1365–like simulation was run for about 6.5 Gyr, keeping the gas warm (5×10^4 K) and isothermal to let the bar structure develop itself (and save CPU time), then followed by more than 1 Gyr of evolution with all subgrid recipes turned on (i.e., cooling, star formation) at maximum resolution.

In the simulation, a first-generation 8 kpc bar develops over the first gigayear, which then weakens between 1 and 2 Gyr, slowly regrowing at later times to reach about 20 kpc length after 6 Gyr. The resulting large-scale bar exhibits an extended central mass concentration of old and young stars, together with large-scale gas lanes wrapping around the central few kiloparsecs, reminiscent of what is observed for NGC 1365. For comparison to the observations, we select by visual inspection a snapshot that broadly resembles the gas intensity and line width distribution in NGC 1365's inner 5 kpc (see Section 4.3). We derive the fractional H_2 mass per cell from the simulation in postprocessing by applying the gas density and metallicity-dependent prescription from Krumholz et al. (2009).

3. Results

As we aim to study the circumnuclear star formation process, we focus our analysis on the inner ~ 5 kpc region of NGC 1365. The analysis of the molecular gas emission encompasses the standard moment maps (Section 3.1) and a kinematic analysis including a parametric decomposition of the gas emission using SCOUSEPY (Section 3.3). The study of the dust emission relies mostly on the JWST/MIRI imaging in the F770W and F1000W filters probing emission from PAHs and (very) small grains that trace the cold ISM and young (embedded) star-forming regions (Section 3.2).

3.1. Properties of the Molecular Gas in NGC 1365's Inner Disk

We show the integrated intensity map (broad mask), peak temperature map (T_{peak}), velocity field (v_{LSR}), and effective width (EW) distribution of the CO(2−1) line emission at ~ 30 pc ($0''$) resolution in Figure 2. The EW is the inferred velocity dispersion from the integrated intensity and peak temperature if the line profile were Gaussian: EW$= I_{CO}/(\sqrt{2\pi}\,T_{peak})$. The CO(2−1) line emission is detected well above 5σ from the inner roughly $50'' \times 35''$ (4.8×3.3 kpc^2). The gas emission is resolved into a bright spiral-like structure that corresponds to the inner ends of the bar lanes seen in molecular gas and dust along the large-scale (28 kpc in diameter) stellar bar (see Figure 1). These bar lanes encompass a lower brightness disk inside a galactocentric radius of $R_{gal} \approx 5''$ that only becomes evident at this resolution. At the location of the nucleus, there is a weak compact peak with an integrated intensity of $I_{CO} \approx 790$ K km s^{-1}. The southern bar lane reaches the northern one, while the northern lane fades at a galactocentric radius of $R \sim 10''$ before reaching the southern one. Although no pronounced lane structure is visible northwest of the nucleus, fainter CO emission is present. While the overall gas morphology is similar to that seen at a lower resolution of $\sim 2''$ in various low-J CO transitions (e.g., Sakamoto et al. 2007; Gao et al. 2021), the bright emission

breaks up into about 13 and five prominent peaks above an integrated surface brightness of $I_{CO} \geqslant 1000$ K km s^{-1} and sizes of $\sim 0''5$–$1'$ in the southern and northern gas lane, respectively. The peak brightness temperature in these integrated emission peaks is mostly well above $T_{peak} = 15$ K. Interestingly, a set of very compact peaks in T_{peak} becomes apparent southwest of the nucleus (but north of the southern bar lane).

The velocity field of the inner low surface brightness disk is very reminiscent of a rotating disk with a position angle close to the value of $\sim 200°$ inferred from the large-scale CO(2−1) velocity field (Lang et al. 2020). Where the bar lanes reach smaller galactocentric radii, the velocity field significantly deviates from circular rotation, implying strong streaming motions (i.e., noncircular motions in the plane of the galaxy; Figure 2). Interestingly, there is no clear or simple correlation between molecular gas surface brightness and velocity field deviation along the bar lanes. This behavior was already visible in the $2''$ lower-resolution data (Gao et al. 2021). However, the abrupt change of the isovelocity contours at the location of, in particular, the southern lane becomes much more evident at $0''3$ resolution.

The ~ 30 pc resolution data reveal a low mean effective line width of $\langle EW \rangle = 14$ km s^{-1} inside $R_{gal} \approx 5''$, i.e., for the inner circular rotating gas disk, with an $\sim 3\times$ higher value at the very nucleus. At the location of the prominent gas lanes, the EW increases significantly and reaches values well above 30 km s^{-1}, particularly in the southern bar lane. High-EW regions are often coincident with the compact integrated brightness peaks, but not always. The mismatch is particularly apparent for the northern bar lane.

3.2. Distribution of PAH and Hot Dust Emission

The JWST/MIRI broadband filters are excellent tracers of the distribution of the ISM, as they probe emission from very small dust grains (heated by single photons), polycyclic aromatic hydrocarbons (PAHs), the hot thermal dust continuum, and, to a lesser degree, light from stars luminous in the near-IR, such as AGB stars (e.g., review by Galliano et al. 2018).

In particular, the F770W filter encompasses emission from the 7.7 μm PAH feature and provides a detailed view of the distribution and morphology of the neutral ISM at its $\sim 0''24$ (~ 23 pc) resolution (e.g., Leroy et al. 2023b; Sandstrom et al. 2023, this Issue). The F770W distribution in NGC 1365 reveals a prominent central disk with filamentary morphology that extends beyond the molecular bar lanes (Figure 3, left). It is interesting to note that only a few shell-like features or bubbles (with diameters of 10 to a few hundred parsecs) are obvious, e.g., west of the northern bar lane. This is in stark contrast to the central 3 kpc of the nearby grand-design spiral galaxy NGC 628, where Watkins et al. (2023) visually identified 569 (presumably stellar feedback–driven) bubbles with a mean diameter of 77 pc. This might suggest that the PAH distribution in NGC 1365's center is not shaped by stellar feedback. The brightest emission ($I_{F770W} > 400$ MJy sr^{-1}) forms a ringlike distribution between galactocentric radii of $R \approx 5''$–$13''$ that roughly coincides with the CO(2−1) emission. However, there are notable differences between the PAH and CO distributions: (a) southwest of the nucleus, bright PAH emission "fills" the ring, while bright CO emission is absent; (b) the southern CO bar lane outside a galactocentric radius of $R \sim 13''$ exhibits bright to very bright CO emission without correspondingly
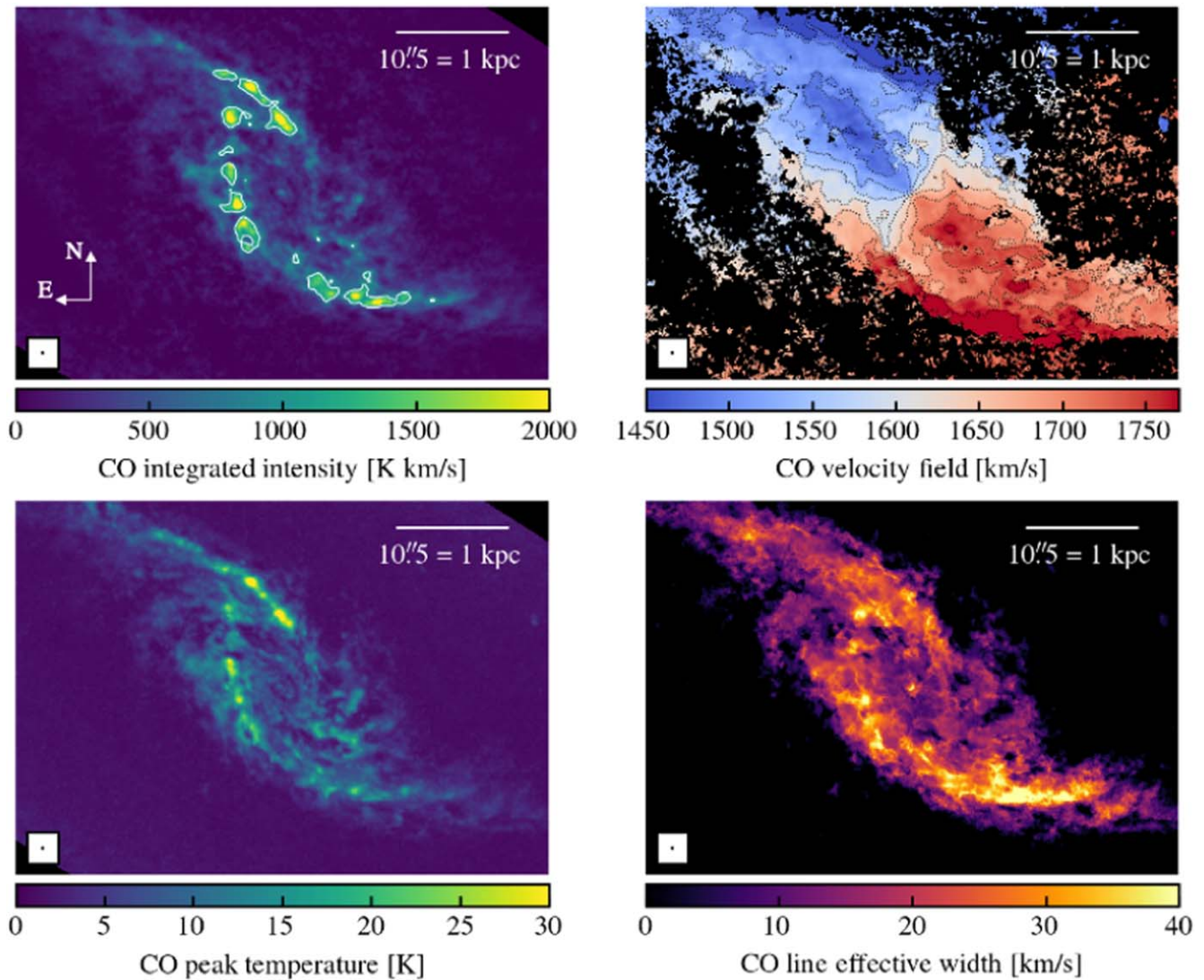
Figure 2. Molecular gas as probed by the CO(2−1) line emission from the inner 4.8×3.3 kpc^2 of NGC 1365 at $\sim$30 pc ($0\rlap{.}''3$) resolution observed by ALMA. In the top panels, the integrated intensity distribution (left) reveals a faint smooth gas disk inside the prominent gas spiral arms. The white contour highlights $I_{CO} = 1000$ K km s^{-1}. The velocity field (right) shows circular rotation in the inner disk and clear deviations from this pattern at the locations of the gaseous bar lanes. The isovelocity contours are in steps of 40 km s^{-1} from the systemic velocity. In the bottom panels, the CO(2−1) peak temperature map (left) reveals several peaks reaching temperatures above 20 K, which often agree with peaks in the integrated intensity. Enhanced EWs (right) roughly coincide with the brightest emission in the bar lanes. The faint emission peak associated with the nucleus shows larger line widths above 40 km s^{-1}.

bright PAH emission; and (c) a linear fainter PAH emission feature about $15''$ to the northeast of the nucleus connects the ring to the northern bar lane without a counterpart in CO emission.

Among the filters used by PHANGS–JWST, F2100W is the most sensitive to emission from hot dust, as it probes the longest-wavelength range where emission from PAHs no longer dominates (also evident from its different scaling to CO emission; see Leroy et al. 2023b). Due to its lower resolution of $\sim 0\rlap{.}''67$ and significant saturation affecting several regions in the central $20''$ of NGC 1365, we resort to the F1000W map, which is less affected by saturation. This filter probes the underlying dust continuum in star-forming galaxies but can be affected by silicate absorption, which is mostly seen in AGN and MIR spectra of ULIRGs (Spoon et al. 2007; Galliano et al. 2018). It typically probes dust heated by single photons (see review by Galliano et al. 2018), although the analysis by Leroy et al. (2023b) suggests a significant

contribution of PAH emission, especially at lower intensities. The overall distribution of the 10 μm emission (Figure 3, right) is as expected, similar to that of the 7.7 μm PAH emission.

In addition, several compact bright sources are evident. We generate a catalog of bright compact sources identified in the F1000W image following the methodology outlined in Hassani et al. (2023, this Issue). They selected bright compact sources at 21 μm, showed that 85% are consistent with being embedded star-forming regions (the remainder are background galaxies ($\sim$10%) or dusty stars ($\sim$5%)), and suggested that the 10 μm emission of these objects is consistent with probing hot dust emission. Selecting only 10 μm–identified sources with $F_{\text{F1000W}} > 100$ and $F_{\text{F2100W}} > 200$ μJy, we obtain a total of 37 compact objects (see diamonds in Figure 3, right). Comparison to ground-based N-band imaging work by Galliano et al. (2005) reveals that all of their seven off-nuclear MIR sources are detected in the JWST map, with sources M5
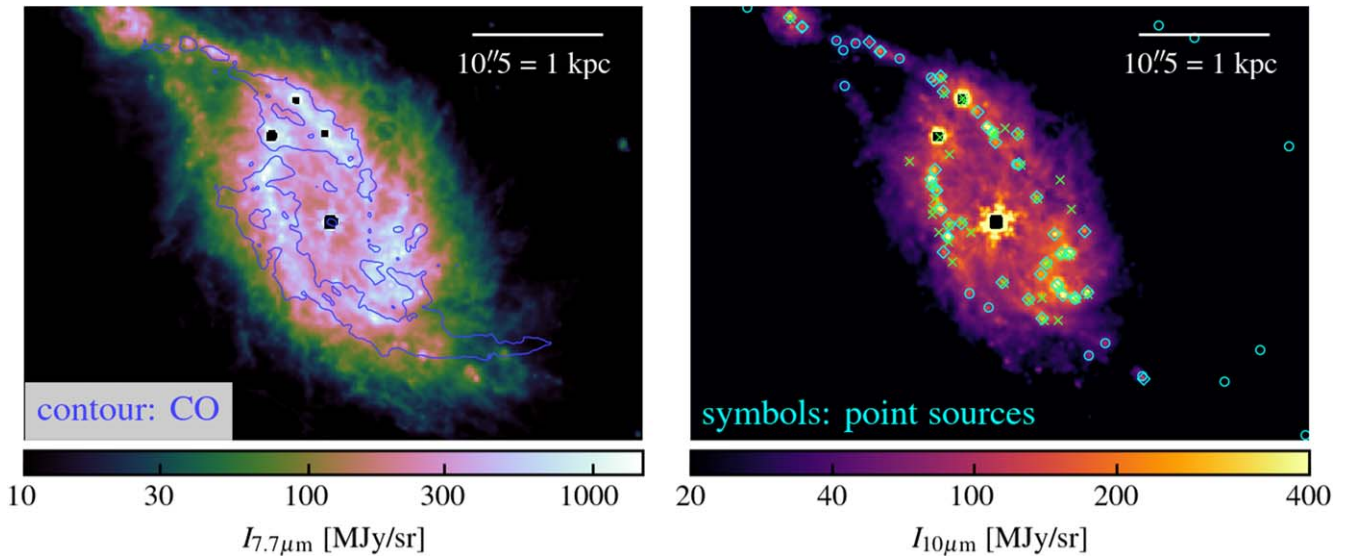
Figure 3. Distribution of the emission from PAHs and hot dust emission as probed by JWST/MIRI observations at $\sim0\!\!''3$ resolution, which is comparable to the resolution of the ALMA CO(2−1) data (north is up, and east is to the left). In the left panel, the F770W filter with an $\sim0\!\!''24$ resolution reveals the overall distribution of the neutral ISM, as its emission is dominated by the 7.7 μm PAH feature. For reference, the distribution of the CO emission is shown by a single blue contour. Note that the central position is significantly affected by saturation due to the bright AGN and dominated by its PSF, causing the artifacts. Also, the three brightest compact sources north of the AGN are saturated. In the right panel, several embedded young star-forming clusters are evident in the 10 μm emission and stand out as bright compact sources. Our 10 μm–selected sources are highlighted by cyan diamonds and only found in the region shown. About 57% of these objects coincide with the young (<10 Myr) star clusters studied by Whitmore et al. (2023b; green crosses) and have estimated stellar masses of $10^6 M_{\odot}$ or higher. The 21 μm–selected sources from Hassani et al. (2023) that are classified as ISM-emitting sources are shown as cyan circles. The dearth of clusters in the bar lane southwest of the nucleus is notable.

and M6 being saturated there (and added by hand to our 10 μm sample).

To assess the completeness of the dusty star-forming regions, we compare our 10 μm–selected sample to the 21 μm–selected embedded cluster candidates from Hassani et al. (2023).[38] There are 18 embedded star-forming cluster candidates with $\nu L_{\nu,21\mu m} = 10^6$–$10^8 L_{\odot}$ present in the molecule- and PAH-bright region.[39] Eight candidates ($\sim45\%$) coincide with our 10 μm–selected sources. The remaining 10 sources are identified at 10 μm by our method, albeit at flux levels below our imposed flux cut, implying that their MIR colors (21–10 μm) are redder. The brightest MIR sources, like M4, M5, M6, and likely a few others southwest of the nucleus, are missing from the 21 μm selection due to saturation.

Whitmore et al. (2023b, this Issue) compiled a sample of 37 young ($T_{Age} \leqslant 10$ Myr), massive ($M_{\star} \geqslant 10^6 M_{\odot}$) star clusters based on a combination of optical (from HST; Turner et al. 2021, Whitmore et al. 2023a), radio (Sandqvist et al. 1995), ground-based (Galliano et al. 2005), and space-based (JWST filters F335M, F770W, and F1130W) MIR observations. The mean age, stellar mass, and attenuation of these sources are $\log(t_{Age}\,\mathrm{yr}^{-1}) = 6.5 \pm 0.2$, $\log(M_{\star}/M_{\odot}) = 6.3 \pm 0.3$, and $A_V = 6.3 \pm 3.4$ mag based on estimates from a combination of HST and JWST information (for details, see Whitmore et al. 2023b). About 21 of these clusters (57%) are in common with our 10 μm–selected sources (when including the saturated M5 and M6 sources), strongly supporting our notion that all 10 μm–identified sources are also likely massive young clusters (Figure 3, right). The three brightest clusters (all badly

saturated in the F2100W filter) are M4, M5, and M6, which are also the three strongest radio continuum sources at 6 cm (Sandqvist et al. 1995). For the brightest off-nuclear sources at 10 μm, M4, M5, and M6, Galliano et al. (2008) quoted ages of ~7 Myr and stellar masses of $\sim10^7 M_{\odot}$ based on MIR spectroscopy, while for the same objects, Galliano et al. (2012) reported ages of $\log(t_{Age}\,\mathrm{yr}^{-1}) \sim 5.5$–$6.5$ and stellar masses of $\log(M_{\star}/M_{\odot}) \sim 6.5$–$7.0$ based on NIR integral field spectroscopy that are consistent with the values of Whitmore et al. (2023b) of $\log(t_{Age}\,\mathrm{yr}^{-1}) = 6.5/6.5/6.5$ and $\log(M_{\star}/M_{\odot}) = 6.0/6.6/6.7$ for M4, M5, and M6, respectively. These discrepancies demonstrate the challenge of obtaining accurate ages for these clusters.

The union of these three catalogs should provide a good representation of the distribution of ongoing massive star formation in the CMZ of NGC 1365 independent of the amount of dust that is present. The distribution of these young (embedded) cluster candidates falls broadly into three categories: (i) delineating very well the gaseous bar lanes northeast of the nucleus (including the MIR-brightest M4, M5, and M6 clusters) with a fair number of JWST-only identified clusters along the northern lane, (ii) a more stochastic distribution southwest of the nucleus, and (iii) a remarkable dearth of clusters in the outer southern CO lane.

3.3. Molecular Gas Dynamics in the Inner 5 kpc

We apply SCOUSEPY (Henshaw et al. 2016, 2019) to the ALMA $0\!\!''3$ CO(2−1) data cube to decompose the emission lines into individual Gaussian components (Figure 4; see the Appendix). Following quality control, $\sim93\%$ of all spectra contained within the masked region have model solutions. The majority of the line emission in the inner 5 kpc is well fitted with a single component, with multicomponent models required for $\sim31\%$ of the spectra. On average, ~1.4

---

[38] Their sources with an "ISM_EYE = true" flag, i.e., they are being visually classified as having their 21 μm emission due to ISM/hot dust and not being a background galaxy or a dusty star.

[39] Another six sources can be seen well outside this region in the west and are disregarded in the further discussion.
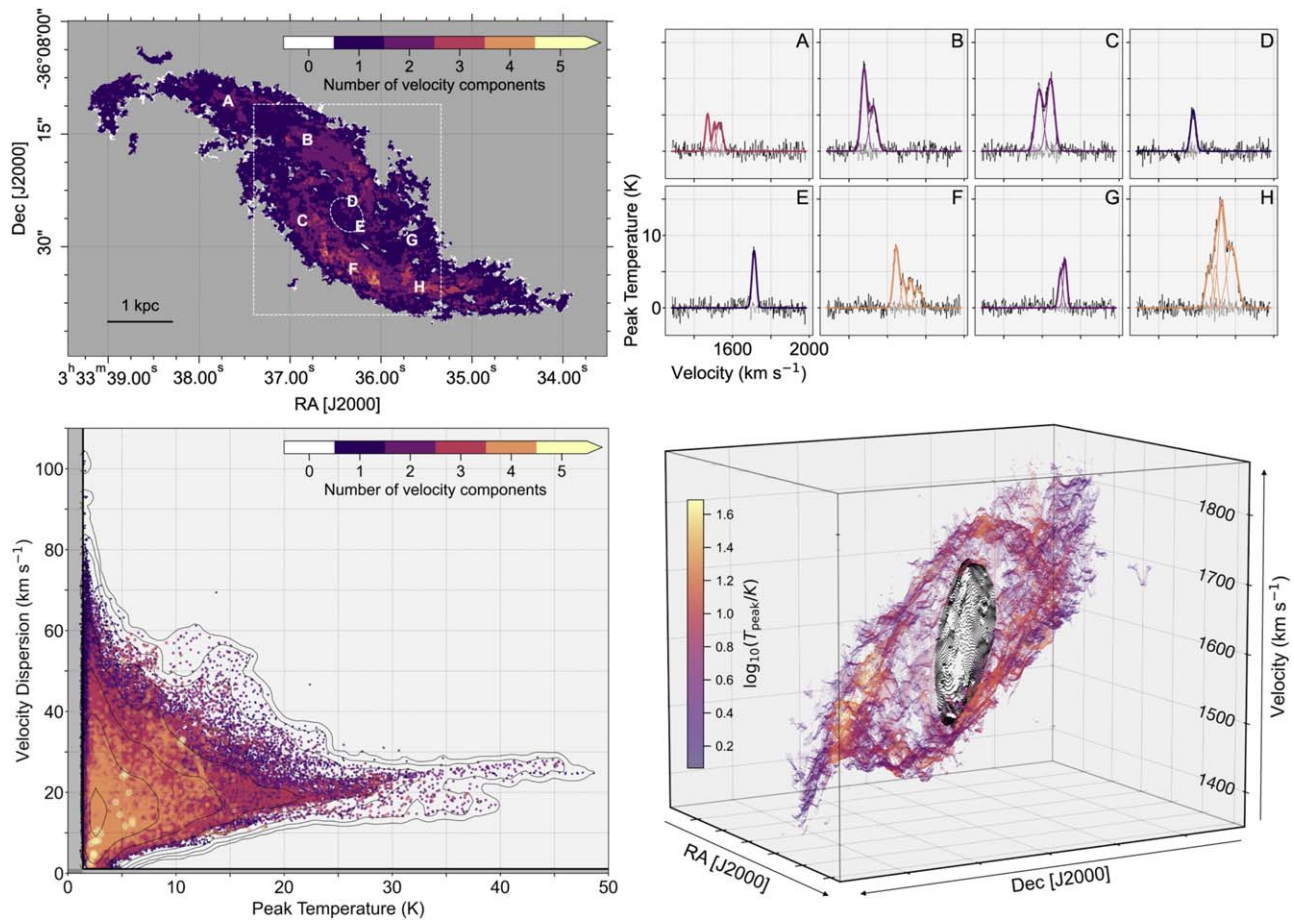
Figure 4. SCOUSEPY decomposition of the 30 pc resolution molecular CO(2−1) gas emission. Multiple Gaussian components are needed to fit ∼31% of the data. This is demonstrated most clearly in the spiral arms, where two- and three-component models are common (up to six components in the southwestern arm; top left). Spectra from selected regions with the resulting SCOUSEPY fits typically exhibit well-separated line components (top right). The inferred peak CO temperature and velocity dispersions of the individual SCOUSEPY components (bottom left) occupy a similar region of parameter space independent of whether they are derived from single or multiple-component fits (color-coding). The gray shaded regions correspond to the limits of our fitting (a signal-to-noise ratio of 2 and a single channel width). The three-dimensional representation of the individual SCOUSEPY components located within the white dashed box in the top left panel, displayed in ppv space (bottom right), reveals an inner smoothly rotating disk (highlighted in black; extracted from the ellipse in the top left panel), while the bar lanes show strong local fluctuations in velocity indicating an increasing complexity of the kinematics in the molecular gas there (the color refers to the peak CO temperature of the individual components). The physical spacing of the position–position grid in this image is ∼475 pc.

components are fit per spectrum (or ∼2.1 in the spectra where multicomponent models are needed). The exceptions to this are the brighter bar lane regions, where two or more components are almost always required. In the regions with high EWs—for example, in the southern lane (top left panel of Figure 2)—four-, five-, or even six-component models are sometimes necessary to describe the data (top right panel of Figure 2). These individual components are distinct features in the line profiles, typically spread over a velocity range of $\approx 125\,\mathrm{km\,s^{-1}}$, with velocity separations of $\delta v \approx 41\,\mathrm{km\,s^{-1}}$ (see the mean measured dispersion of these components of $\approx 17\,\mathrm{km\,s^{-1}}$). The relative motion between these distinct peaks can help to drive an increase in the measured EW at these locations, and this velocity separation suggests significant intercloud motion.

Although the spread in measured quantities is large, the distributions of the inferred integrated line intensities and velocity dispersions are reasonably similar for single and multiple-component fits. As can be seen in Figure 4 (bottom left panel), single and multicomponent models occupy a similar region in peak temperature–velocity dispersion space. The median peak temperature (amplitude of the Gaussian fit), integrated intensity (integrated Gaussian), and velocity

dispersion (sigma of Gaussian fit) are $T_{\mathrm{peak}} = 3.6^{+4.1}_{-1.5}$ K, $I_{\mathrm{CO}} = 77.8^{+88.9}_{-42.0}$ K km s^{-1}, and $\sigma = 18.6^{+11.1}_{-7.2}$ km s^{-1}, where the upper and lower limits here represent the 16th and 84th percentiles, respectively. We convert the CO intensity of each individual SCOUSEPY component to H_2 surface density using the information outlined in Section 2.1 and the conversion $R_{21} = 1$ outlined in Leroy et al. (2023a). The median value for individual components is $\Sigma_{H_2} \sim 800^{+916}_{-432} M_\odot \mathrm{pc}^{-2}$. Both the median velocity dispersion and the surface density of the components are similar to those found in the CMZ of the Milky Way (Henshaw et al. 2022).

The bottom right panel of Figure 4 shows the three-dimensional position–position–velocity (ppv) distribution of the individual velocity components (those located within the white dashed box in the top left panel). The color corresponds to the peak brightness temperature of the fitted components in the bar lanes, and we highlight in black all velocity components within an ellipse (with semimajor and semiminor axes of $2''5 \times 2''$ or 240 pc × 190 pc, respectively; see top left panel) centered on the nucleus (in the plane of the sky). The velocity structure of these highlighted components is consistent with a dynamically cold, circularly rotating gas disk; i.e., the
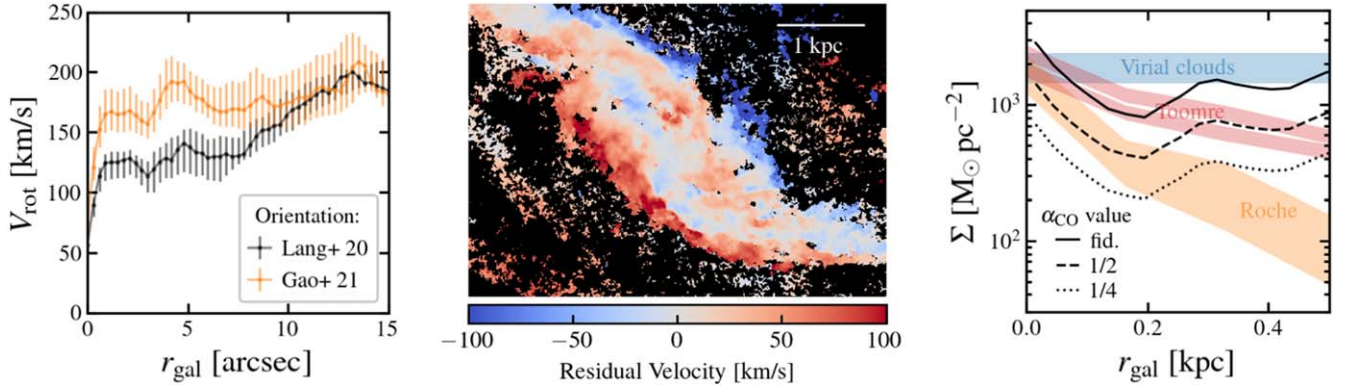
Figure 5. In the left panel, refined molecular gas rotation curves using the 0″3 CO velocity field are shown using the orientations from Lang et al. (2020; PA = 201°, inclination = 55°; black curve) and Gao et al. (2021; PA = 220°, inclination = 40°; orange curve). In the middle panel, the resulting residual velocity field when removing a circularly rotating disk (based on the inferred rotation curve using the Gao et al. 2021 orientation) clearly reveals strong streaming (i.e., noncircular) motions at the location of the gas lanes. In the right panel, the radial profile of the median molecular gas surface density (nominal curve: black solid line, assuming a 2 or 4× lower CO-to-H₂ conversion factor: dashed and dotted lines, respectively) is compared to a number of stability criteria: virialized clouds (blue), Toomre critical density (red), and Roche density (orange). The gas in the inner disk ($R_{\rm gal} \leqslant 5''$) is basically stable against gravitational collapse for all criteria considered (see text for details).

components follow a thin two-dimensional plane in ppv space. In contrast, the bar lanes display a comparatively complex velocity structure, with 5–10 km s⁻¹ local velocity fluctuations superposed on the large-scale (ordered) noncircular motions. The warp-like appearance in ppv space is consistent with streaming motions. These complex local fluctuations may be driven by a combination of physical mechanisms (e.g., noncircular gas flows and colliding flows), and in-depth analysis of these goes beyond the scope of this initial paper. However, we note that they are qualitatively similar to those detected ubiquitously across all scales in the ISM, both in nearby galaxies and in the Milky Way (Henshaw et al. 2020).

We fit the 0″3 resolution CO velocity field using the software developed by Lang et al. (2020) in order to refine the rotation curve of Lang et al. (2020), particularly at small galactocentric radii ($R < 20''$; see Figure 5, left). As the derived rotation curve is less reliable for radii beyond the inner disk that are affected by strong streaming motions, we only show the rotation curves out to $R_{\rm gal} \approx 15''$.

Two orientations are considered: the orientation used by Gao et al. (2021; PA = 220°, inclination = 40° from Sakamoto et al. 2007) and the orientation fitted at 150 pc resolution (PA = 201°, inclination = 55°) by Lang et al. (2020).[40] For reference, we note that the circular velocity measured in the innermost 30 pc bin in both cases is consistent with the expected motion around a central black hole with mass in the range $\log M_{\rm BH}/M_\odot = 7-8$ estimated for this galaxy given its stellar mass and adopting the $M_{\rm BH}$–stellar mass scaling relation measured by van den Bosch (2016).

For direct comparison to Figure 6 of Gao et al. (2021), the residual velocity field shown (Figure 5, middle) adopts their orientation parameters. The pattern of residuals in the inner disk is consistent with a rotating disk but shows evidence that either the adopted inclination is incorrect or, alternatively, the gas is still moving on elliptical orbits associated with the bar potential. Toward larger galactocentric radii, strong

noncircular, streaming motions associated with the bar lanes are well separated from the inner disk and consistent with those shown by Gao et al. (2021). A full kinematic analysis combining information across the full gas disk from atomic and molecular gas data would be able to address these open points, but it is beyond the scope of this paper.

We derive dynamical timescales of $T_{\rm dyn}(R = 5'' \approx 475\,{\rm pc}) \sim$ 15–30 Myr and $T_{\rm dyn}(R = 10'' \approx 950\,{\rm pc}) \sim 36-40$ Myr from the orbital period at these radii. These short timescales imply that the morphology seen in cold gas, dust, and star formation (tracers) can evolve quickly, and they are comparable to the timescales inferred for the gas cycling of molecular clouds (Kruijssen et al. 2019; Schinnerer et al. 2019; Chevance et al. 2020; Kim et al. 2022; Pan et al. 2022; Ward et al. 2022).

To assess the stability of the inner gas disk against gravitational collapse, we compare the molecular gas surface density to three reference critical densities: the Roche density (Tan 2000) for tidal stability on the beam scale (30 pc),

$$\Sigma_{\rm tidal} = \frac{r_c}{R}\left(\frac{V_c^2}{R} - \frac{dV_c^2}{dR}\right); \qquad (1)$$

the Toomre critical density (for stability with Toomre parameter $Q = 1$; Toomre 1964),

$$\Sigma_T = \frac{\sigma\kappa}{\pi G}, \qquad (2)$$

in terms of the radial epicyclic frequency $\kappa^2 = 2\Omega^2(\beta - 1)$, where $\Omega = V_c/R$ and $\beta = dlnV_c/dlnR$; and the surface density needed for uniform density spherical clouds with sizes $r_c \approx 30$ pc (one beam) to reach virial equilibrium (with virial parameter $\alpha_{\rm vir} = 1$; Bertoldi & McKee 1992),

$$\Sigma_{\rm vir} = \frac{5\sigma^2}{\pi G r_c}. \qquad (3)$$

To estimate the Toomre and Roche critical densities, which both depend on the rotation curve, we have used the rotational velocities newly fitted at 0″3 adopting the Gao et al. (2021) and Sakamoto et al. (2007) orientation, as well as the rotational velocities fitted by adopting the Lang et al. (2020) orientation. The radial derivatives of each rotation curve are calculated with windowing to penalize fluctuations that are inherited with the

---

[40] Determination of the position angle and inclination from kinematics is not straightforward for NGC 1365 due to the presence of strong noncircular motions associated with the bar plus outer spiral arms (e.g., in the CO(1–0) velocity field; see Figure 30 of Morokuma-Matsui et al. 2022) and NGC 1365 being the most massive member of a subgroup of the Fornax cluster (Loni et al. 2021).

discrete nature of the measurements. The uncertainty associated with the choice of rotation curve denotes a spread in the estimated values at a given galactocentric radius.

For the Toomre and virial reference surface densities, we consider a range of 30 pc scale velocity dispersions $\sigma = 14-18$ km s^{-1} based on the typical single-component dispersions fitted by SCOUSEPY in the region. This range introduces a spread in the virial density at a given radius. The upper and lower values of the adopted σ define two estimates of the Toomre critical density, each otherwise dominated by rotation curve uncertainty.

As can be seen in Figure 5 (right), the gas surface density lies consistently below the reference stability thresholds inside 300 pc, especially when the conversion factor is 2–4× lower (see Section 2.1). To identify the exact mechanism responsible for preventing the molecular gas from collapsing requires further in-depth analysis, e.g., taking into account the gas structure.

4. Discussion

Using new ∼30 pc resolution observations of the molecular gas in CO(2−1) from ALMA and dust emission from JWST/MIRI, we establish a picture of the star formation process in the past ∼10 Myr (as traced by the young star clusters) in the inner ∼5 kpc of NGC 1365's disks. One of our key findings is evidence for rapid time evolution in the gas distribution and its impact on the present-day distribution of star formation. We see regions undergoing intense massive star formation and some regions that do not appear to be forming stars at all. Before summarizing the main properties of these regions in Section 4.2, we highlight the relevant aspects of the dynamics of the bar environment, assembled from the CO observations analyzed in this work (Section 4.1). The star formation appears sensitive to the current molecular gas distribution that is expected to rapidly evolve in the central regions of the bar given orbital dynamics and strong inflows (see also Sakamoto et al. 2007). In Section 4.3, we leverage hydrodynamical simulations of a galaxy with properties similar to NGC 1365 to support this view, in contrast to other work suggesting (at least partially) that the AGN outflow piles up the gas and induces star formation (Gao et al. 2021; also discussed in Section 4.2.3).

4.1. Gas Flows and Turbulent Motions in the Bar

We can gain insight into the nature of star formation in the bar by considering the observed molecular gas properties in the context of bar dynamics. Gas flows along the so-called x_1 bar orbits and the set of perpendicular x_2 orbits, which form a ring or ellipse (see Figure 1) evident in the F770W map. The transition from x_1 to x_2 orbits leads to the development of the bar lane shocks along the bar leading edge (the northern and southern bar lanes), where gas is funneled toward smaller radii (Athanassoula 1992; Sormani et al. 2015).

The fueling of the central ringlike structure by gas from larger radii appears to be at least partially responsible for the complex kinematics in the region as revealed by the SCOUSEPY decomposition. Gas arriving at the ring shares the same high level of complexity present in the northern and southern bar lane arms (described more below; see Figure 4). In addition, the ongoing massive star formation in the ringlike structure is also injecting a large amount of energy via stellar feedback. The disappearance of the complex velocity structure toward smaller

galactocentric radii suggests that the sources contributing to the complex velocity structure are changing toward smaller radii (see Section 5).

Further out (beyond the inner $R_{\rm gal} \geqslant 12''$) in the northern and southern bar lanes that run along the large-scale bar (Leroy et al. 2021a; Egusa et al. 2022), overlapping gas streamlines lead to more complex gas kinematics, often with multiple peaks observed along the same line of sight. Ongoing massive star formation, meanwhile, is distributed in an asymmetric fashion along the bar lanes, with many cluster candidates associated along the full length of the northern lane, while the southern lane lacks clusters at larger radii despite fairly high integrated CO intensities. There is a broad age trend when going from large to small galactocentric radii along the bar lanes.

In the northern lane (see Figure 6), the highest integrated CO intensity coincides with the highest attenuation and brightest MIR clusters at large radii, whereas low CO intensity is colocated with the brightest observed Hα emission and a clustering of young clusters at smaller radii. Further molecular gas properties in that region are consistent with more diffuse, warm gas relative to the rest of the ring (Liu et al. 2023); this is consistent with this region having experienced star formation for a longer amount of time. For the southern lane, the lack of star formation in the outer part of the lane, together with the high attenuation, implies that this region is less far along in the star formation process than the inner part, where many clusters are seen and attenuation is low. The time difference between the two bar lanes is about 10 Myr when considering only the dynamical time. It is interesting that while a rough time sequence is evident along both bar lanes, it is not exactly mirrored, as the southern lane contains molecular gas before the onset of massive star formation.

4.2. Gas, Dust, and Star Formation at 30 pc Resolution

The inner 5 kpc of NGC 1365 can be divided into two broad regimes given its molecular gas and star formation properties (see Figure 6): those exhibiting no/low star formation (central smooth disk, outer southern bar lane) and those exhibiting a high abundance of young massive clusters (massive star-forming region southwest of the center, stringlike star formation northeast of the center).

We expect these regions to be common to the CMZs of other barred galaxies, although their occurrence could depend on the exact geometry of the underlying bar orbits, the distribution of gas along the bar, and the time when the system is observed. We thus give an overview of the basic properties of these regions and comment on how they support our view of rapid evolution in the gas and star formation distributions in the bar region. We also comment on the nature of the central starburst.

4.2.1. Low Star Formation Regions

The absence of massive young star clusters is evident for the inner 1 kpc, as well as the outer part of the southern molecular bar lane.

Central smooth disk—We find no evidence of ongoing massive star (cluster) formation inside a galactocentric radius of $R_{\rm gal} \approx 5''$ (475 pc), where a dynamically cold, regularly rotating molecular gas disk has been identified. Figure 7 shows an image of the western inner "spiral-like" feature near the nucleus of NGC 1365 (see also Whitmore et al. 2023b). We find that while it breaks down into hundreds of individual
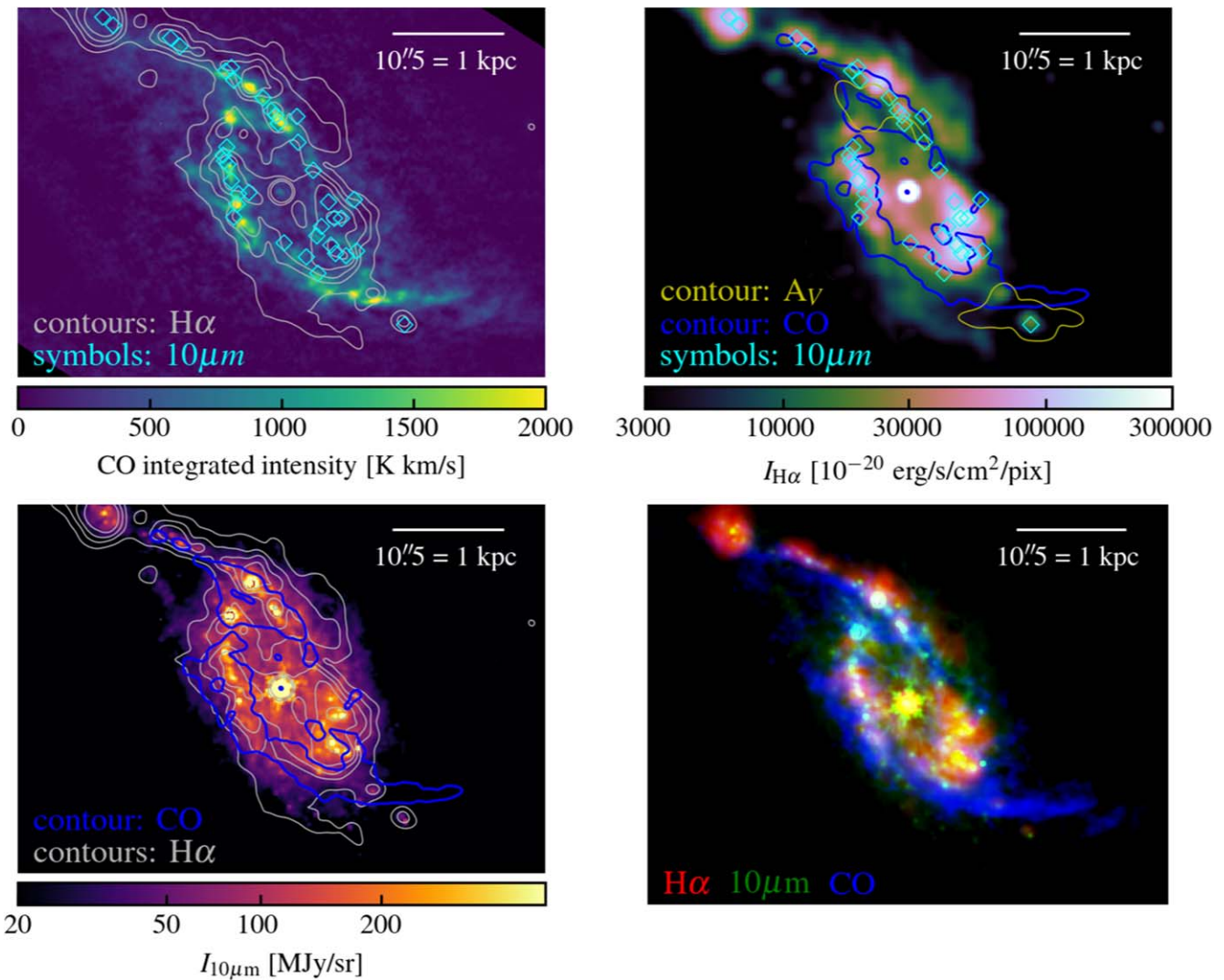
Figure 6. Comparison of the distribution of the molecular gas and sites of ongoing star formation in the central ∼5 kpc of NGC 1365 in four different representations (north is up, and east is to the left). The ALMA CO(2−1) integrated intensity map (in color in the top left panel, in blue in the bottom right panel, and as blue contours in the remaining panels) basically traces the immediate gas reservoir for star formation. The JWST/MIRI 10 μm continuum map (in color in the bottom left panel and green in the bottom right panel) shows where the bright compact regions (cyan symbols, top panels) are likely tracing young (≲10 Myr) massive (≈$10^6 M_\odot$) star-forming regions. The PHANGS–MUSE Hα emission line map (Emsellem et al. 2022) at 1″15 resolution (in color in the top right panel, in red in the bottom right panel, and as gray contours in the remaining panels) reveals the location of bright H II region complexes that are ionized by massive O stars. Regions of high attenuation ($A_V \gtrsim$ 4 mag; Belfiore et al. 2022) are indicated by a yellow contour.

pointlike objects in the F200W map from PHANGS–JWST (Lee et al. 2023), it remains patchy and nebulous in the F814W image from PHANGS–HST (e.g., Lee et al. 2022, Whitmore et al. 2023b). There is only one object along the feature that is bright enough to be a regular, low-mass cluster (i.e., ∼$10^5 M_\odot$; B. Whitmore, private communication). We speculate that either massive clusters, like those that exist just a few hundred parsecs away in great number, cannot form in this environment, or, perhaps more likely, the massive clusters formed at larger radii are destroyed by tidal forces, leaving the debris of large numbers of individual stars in their wake in a visibly smooth-looking pattern (similar to the scenario proposed for the massive star clusters in the Milky Way CMZ by Habibi et al. 2014). We note that the hundreds of faint, crowded, pointlike objects along the western inner spiral have F200W fluxes similar to red supergiant stars with ages around 10 Myr seen in the outer parts of the galaxy, but since they are not resolved in the visible or at longer wavelengths due to

available spatial resolution, it is difficult to determine their color and thus true nature.

The mean integrated CO(2−1) intensity in the inner 1 kpc is $\langle I_{\mathrm{CO(2-1)}} \rangle \approx 300$ K km s^{-1}, which corresponds to gas surface densities of $\Sigma_{\mathrm{H_2}} \approx 1300 M_\odot \mathrm{pc}^{-2}$ assuming a Galactic conversion factor and $R_{21} = 1$ (see Section 2.1). Lowering the conversion factor by 2–4× (Teng et al. 2022) still results in sufficiently high surface densities for star formation to happen. However, rough estimates of critical densities for stability (see Section 3.3) suggest that even at these high gas surface densities, the gas is stabilized against gravitational collapse. Overall, these properties are similar to the central molecular disk in our own Milky Way, where it has been suggested that high shear can dissolve and disrupt clouds (e.g., Hatchfield et al. 2021) and act to counter gas self-gravity (Meidt et al. 2018; Li & Zhang 2020). The central region is also reminiscent of the situation in early-type galaxies, where strong shear is able to oppose self-gravity (Liu et al. 2021) and prevent the
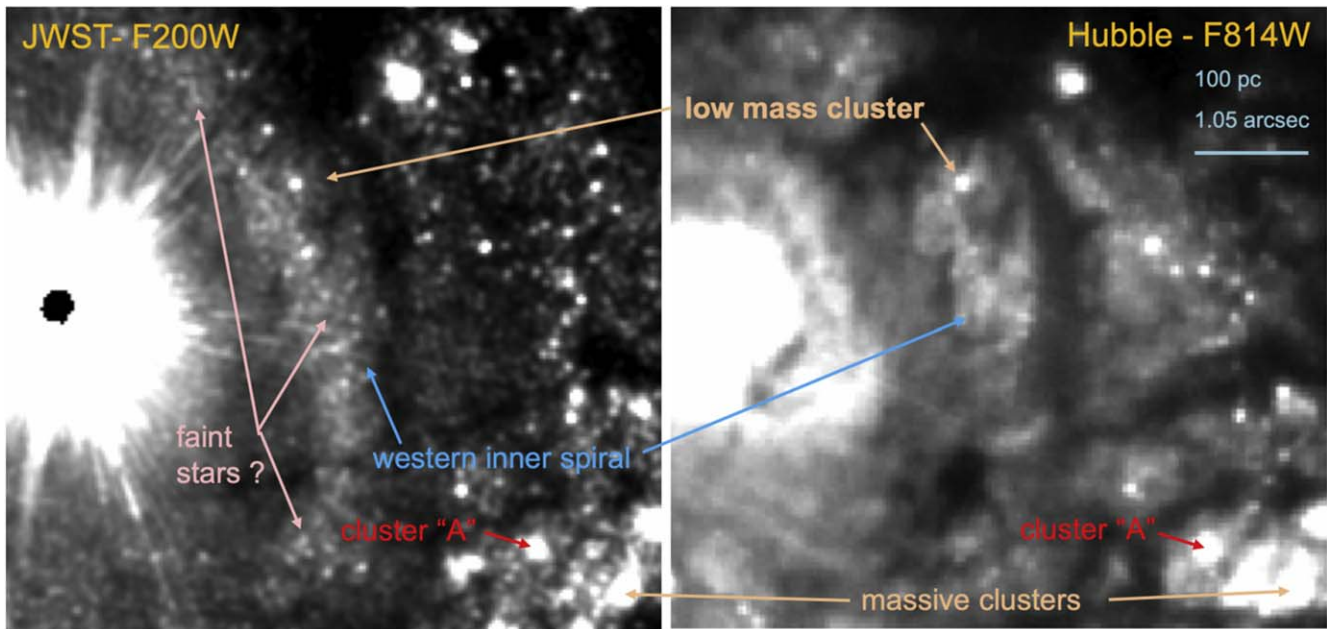
Figure 7. Close-up look ($5'' \times 5''$) at stellar populations in the inner disk (north is up, and east is to the left). The high sensitivity and resolution of the JWST/NIRCAM F200W imaging from PHANGS–JWST (left; Lee et al. 2023) reveals more structure in the region where undisturbed circular rotation gas has been found compared to what can be seen in the HST F814W map (right; Lee et al. 2022; Whitmore et al. 2023b, Whitmore et al. 2023a). Different regions that are discussed in the text are annotated. The bright (saturated) source to the east is the AGN at the center of NGC 1365.

fragmentation of the gas disk (Gensior et al. 2020), thus suppressing the formation of massive stars (Davis et al. 2022). This would mean that star formation in the inner 1 kpc is suppressed over long timescales.

Outer southern bar lane—There is much reduced ongoing massive star formation in the outer southern bar lane (only two $21\,\mu$m–selected regions but no $10\,\mu$m–identified cluster candidates and only one Hα emission peak being a H II region; see Figure 6). The apparent lack of corresponding $7.7\,\mu$m PAH emission (see Figure 3 left) is puzzling. We speculate that this could be related to the lack of heating sources (see outer part of northern bar lane), as there is only one Hα peak that has $E(B-V) \approx 1.7$ mag (or $A_V \approx 5.3$ mag). In contrast to the central disk discussed above, this lack of star formation points to a timing issue (see also Section 4.3). While we observe the highest CO velocity dispersion (coincident with high integrated CO intensity but only average peak temperatures; see Figure 2) in this region, the SCOUSEPY decomposition shows that the high dispersion arises due to multiple line components that have peak temperatures and line widths consistent with the remaining molecular gas (see Figure 4). Thus, we can rule out enhanced turbulence as the cause for the lack of star formation. Taken together, this suggests that this region is the youngest (relatively speaking) region in the inner part where star formation has not yet turned on. Hydrodynamical simulations of barred galaxies show a rapid evolution in the gas distribution in their CMZs (Sormani et al. 2020; Tress et al. 2020; see also Section 4.3).

The absence of ongoing massive star formation has different origins in the two regions discussed above. While in the central disk, there are factors that can genuinely suppress star formation, the situation for the outer southern bar lane could be just a timing issue, given that the molecular gas properties are not different from the northern bar lane that hosts abundant young star clusters (see Sections 4.3 and 5). Thus, one needs to be cautious when interpreting such results, especially since

there is abundant massive cluster formation in the remaining parts of the CMZ.

4.2.2. High Star Formation Regions

It is notable that all 37 cluster candidates identified at $10\,\mu$m coincide with regions of notable Hα emission (above $10^{16}\,\mathrm{erg\,s^{-1}\,cm^{-2}\,spaxel^{-1}}$), suggesting that H$\alpha$ emission is a very good indicator of the location of active star formation, and almost no sites of highly embedded star formation are missed even in the gas-rich southern lane (Figure 6, top right). This spatial coincidence is not surprising given the high coincidence ($>90\%$) of $21\,\mu$m–selected ISM sources with PHANGS–MUSE H II regions (Hassani et al. 2023); the good correlation between CO, Hα, and MIRI (F770W, F1000W, F1130W, and F2100W) emission using $\sim$100 pc–sized pixels (Leroy et al. 2023b); and the significant overlap ($\sim$70%) between $24\,\mu$m ($21\,\mu$m) and Hα-emitting timescales (Kim et al. 2021, 2023, this Issue). The distribution of young clusters and massive star formation can be divided in two groups.

Massive star formation southwest of the center—The relatively smooth distribution of the brightest $7.7\,\mu$m PAH emission (see Figure 3) suggests that cold gas has been accumulating at the CMZ for some time. There are two interesting regions along this PAH "ring." First, there is a clustering of 10 ($\sim$30%) young massive star cluster candidates identified at $10\,\mu$m across radii of $5''$–$10''$ at the inner end of the northern bar lane, i.e., southwest of the nucleus just north of the outer southern molecular gas lane. This region exhibits only faint CO emission and is the location of the brightest observed Hα emission indicating the presence of massive H II region complexes (see Figure 6, top row). Liu et al. (2023) studied the molecular gas excitation in the central 5 kpc at $\sim$330 pc resolution and found evidence for low-density warm molecular gas being the dominant phase in this southwest region. Taken together, this suggests that the star formation in this region has

significantly impacted the surrounding cold molecular gas and might be, relatively speaking, the most evolved in time.

Stringlike star formation northeast of the center—Along both bar lanes northeast of the nucleus, cluster candidates closely follow the bright CO ridges, but they do not always coincide with peaks in CO emission, and two-thirds of all $10 \mu m$–selected candidates are located here (Figure 6, top left; see also Figure 3, right). Observed Hα emission from this area is fainter than in the region southwest of the nucleus discussed above; however, attenuation inferred from the Balmer lines (Hα, Hβ) reaches values above $A_V = 4$ mag, where both bar lanes appear to connect and the brightest (saturated) $10 \mu m$ clusters are located. The inferred SFR surface density map, i.e., Hα emission corrected for attenuation, clearly shows that massive star formation ($\Sigma_{\rm SFR} > 1 M_\odot \, {\rm yr}^{-1} \, {\rm kpc}^{-2}$) is confined to the CO ridges and the southwest region. Interestingly, the inner end of the southern bar lanes shows much less attenuation ($A_V \lesssim 2.5$ mag). Given the close morphological relation between the CO ridgelines and the distribution of the massive cluster candidates, we speculate that the observed clusters are still fairly close to their formation sites.

It is interesting to note that star cluster candidates are found along the outer northern bar lane, i.e., outside the PAH "ring," implying that the conditions for massive star formation to occur are already met in the northern lane outside the inner structure. Whitmore et al. (2023b) suggested that the large populations of somewhat older star clusters, with ages between 20 and 400 Myr, that are found slightly outside the northern bar lane originally formed along the bar at larger galactocentric radii. Due to the dynamical decoupling of these stellar clusters from the gas flow along the bar (and onto the ring), these populations are now residing in the so-called overshoot region (see also Figure 1, bottom right). It is conceivable that the currently young clusters could be the precursors of such a population of clusters in a few tens of megayears.

4.2.3. On the Origin of the Starburst and Role of AGN Outflow

Boker et al. (2008) proposed two scenarios on how star formation might proceed within a starburst: (a) a pearls-on-a-string scenario, where star formation is preferentially triggered at or close to the location where the gas lanes along the large-scale bar connect to the inner gas structure, and (b) a popcorn scenario, where star formation occurs stochastically within the ring with no age trend. The rough age trend for overall star formation present along the bar lanes—from star-forming molecular gas to star formation heated molecular gas in the northern lane, from non-star-forming molecular gas to star-forming molecular gas in the southern one. This points toward an evolution of the star formation process along the gas lanes, as expected for the pearls-on-a-string scenario. However, there is no preferred triggering point; rather, star formation already starts before the gas reaches the so-called contact point (see northern lane) or well after it enters the inner structure (see southern lane). The dynamical time of 10 Myr for one gas lane of the ring is sufficiently long that age trends among individual star clusters can be used to more robustly discriminate between the two scenarios when more accurate age estimates based on spectral energy distribution fitting become available in the future.

Object NGC 1365 hosts a large ($r > 2$ kpc) biconical outflow in ionized gas that is likely driven by its central AGN (e.g., Jorsater et al. 1984; Edmunds et al. 1988; Hjelm & Lindblad 1996; Lindblad et al. 1996; Lindblad 1999; Lena et al. 2016; Venturi et al. 2018). Gao et al. (2021) suggested that this outflow is impacting the molecular gas disk based on the analysis of $\sim 2''$ CO(1–0) imaging and affecting the star formation activity in the starburst ring. Our results do not favor such a scenario.

The inner ($R_{\rm gal} < 5''$) dynamically cold unperturbed central gas disk is consistent with circular rotation. The SCOUSEPY decomposition reveals no evidence for second line components that could be associated with the outflow impacting the molecular disk (see, e.g., M51; Querejeta et al. 2016), which is consistent with Combes et al. (2019), who found no evidence for a molecular outflow in their $\sim 0''\!.1$ resolution CO(3–2) data. The on-sky orientation of the outflowing ionized gas is in a fanlike geometry to the southeast and northwest of the nucleus (e.g., see Figure 6 in Venturi et al. 2018). This would imply that molecular gas in the bar lanes discussed here is not impacted in their outer parts. We see no evidence for a change in the characteristics of the complex gas structure revealed by SCOUSEPY in Figure 4 along the gas lanes; i.e., the complexity is similarly high along the full range of gas lanes probed. Further, there is no variation in the distribution of the $7.7 \mu m$ PAH emission. Lastly, Liu et al. (2023) found the CO excitation and CI/CO line ratio to be consistent with star-forming regions in the disk.

Taking all points together makes it highly unlikely that the AGN is impacting the molecular gas in the central region and implies a scenario where the outflow is more aligned with the rotation axis, so that it is not even grazing the molecular gas disk. This is consistent with the three-dimensional cone model of Hjelm & Lindblad (1996) based on fits to ionized gas emission lines. Their inferred cone axis is within 5° of the galaxy's rotation axis, so that the cone is pointing perpendicular to the galaxy disk with an opening angle of 100°.

4.3. Evolution of Gas and Star Formation Distribution

In the following, we compare the observed properties to a RAMSES simulation of a galaxy with global properties matched to NGC 1365 (see Section 2.4). A snapshot resembling NGC 1365's inner gas distribution is shown in Figure 8 (top middle panel). The asymmetric gas morphology consists of a prominent southern gas lane along the bar that extends almost to the northern lane, a shorter northern lane, an additional gas filament located between both lanes northeast of the center, and an inner smooth gas disk plus a couple of compact gas peaks. Similarly, the distribution of young stars with ages of <10 Myr is not very symmetric, with most star formation having occurred northeast of the nucleus. Star formation has been clustered, and the number of stars formed varies significantly between different sites with more prominent locations to the northeast. Young stars are mostly found along the ridgelines of the gas lanes and are associated with peaks in the gas distribution but sometimes away from the lanes. This is illustrated by a few small clusters forming in the southern gas lane in possibly Kelvin–Helmholtz instability-driven structures (e.g., Renaud et al. 2013; see also Mandowara et al. 2022). Along the southern lane, young stars are much more sparse at large galactocentric radii, and the few present coincide with gas spurs emanating from the gas arm. In the northern lane, four big clusters of a few 10^6 and $10^7 M_\odot$ are evident. Inside the smooth central disk (radius of about 300 pc), individual star particles are seen, mostly originating from accreted and
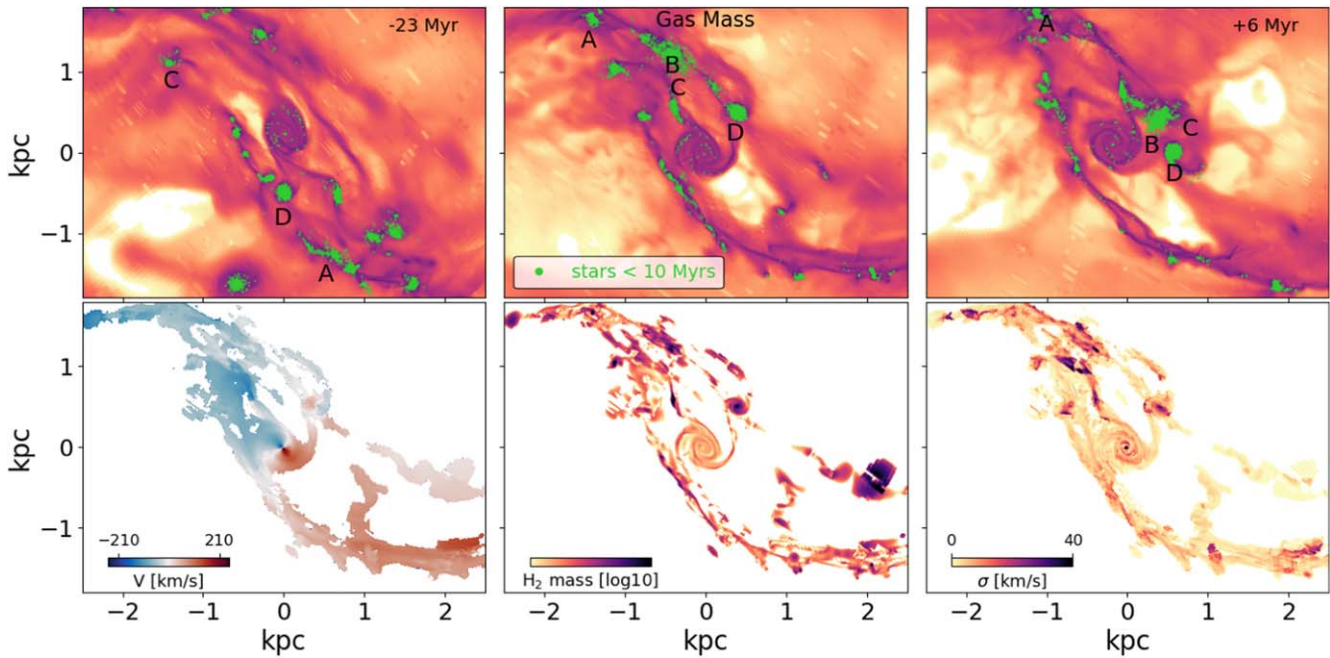
Figure 8. Projected gas density and kinematic maps from a hydrodynamical simulation of a barred galaxy with NGC 1365–like properties. The selected snapshot broadly matches the properties of the gas in NGC 1365's inner disk. The central 5×3.5 kpc^2 with the large-scale galactic bar position and disk orientation on sky matched to NGC 1365's properties. Top row: distribution of the gas mass (color) and stars formed in the past 10 Myr (green points) for the selected snapshot (middle). Comparison to two epochs showing the distributions 23 Myr earlier (left) and 6 Myr later (right) reveals the fast evolution of the morphology in just $\sim$30 Myr, which roughly corresponds to the dynamical time at a galactocentric radius of $R_{\rm gal} = 1$ kpc. Four prominent star clusters are labeled in the panels. The bottom row shows the properties of the molecular H$_2$ gas: gas velocity field (left), H$_2$ gas mass distribution (middle), and H$_2$ gas velocity dispersion (right).

stripped clusters. The overall resemblance to the observations is striking, as the simulation shows a similar asymmetry in the gas distribution and the location where massive star formation occurs in the "starburst ring" and the additional inner smooth gas disk. We note that no bubbles are apparent in the simulations (see the two bubbles at large radii in the northern lane noted by Whitmore et al. 2023b).

We compare gas mass and young star distributions across 30 Myr, which is equivalent to the dynamical time at $R_{\rm gal} = 1$ kpc in NGC 1365 (Figure 8, top row), to gain insights into how transient these morphologies are. After 6 Myr, the northern bar lane becomes more apparent as the filament between the arms has disappeared (right panel). The change in morphology is even more evident in the young stars, where the most prominent location is now just west of the inner gas disk, while the overall location of smaller sites has shifted along the bar lanes. Inspection of the snapshots shows that the four prominent star clusters (labeled in Figure 8) are streaming inward together with an associated gas reservoir. The comparison to 23 Myr earlier is more drastic, as the gas mass morphology does not even represent gas lanes or a ringlike structure. The vast majority of young stars can be found southwest of the nucleus. Despite these stark changes in the gas mass distribution, star formation is always clustered and mostly associated with gas peaks, something that is certainly significantly influenced by the choice of a star formation threshold and unlike what is seen in the observations (see further discussion in Section 5). The rapid evolution of the gas and star formation distribution at any given point in time can be traced back to an irregular and asymmetric gas flow to the inner region. This means that the underlying orbital structure for the gas flow remains stable (e.g., Sormani et al. 2020), while its

population with gas is strongly affected by the fragmentation of the gas disk well outside the inner region studied here.

We show for comparison to the observations the synthetic H$_2$ gas mass distribution, velocity field, and velocity dispersion derived from the matching snapshot (Figure 8, bottom row). The asymmetry in gas morphology is more evident now, as only the densest regions remain. The inner smooth gas disk is fainter, i.e., less massive, compared to the gas in the bar lanes. Similarly, the inner disk is consistent with regular rotation, while strong noncircular motion is evident in the gas lanes. This abrupt change from circular rotation to streaming motions is also present in the simulations of the Galactic center by Tress et al. (2020), implying that this is a common feature in modern hydrodynamical simulations of the central regions of barred galaxies. The highest velocity dispersion regions almost all coincide with regions where many young stars are present. The exceptions are two locations in the western end of the southern arm, where higher dispersion is seen slightly offset from star-forming sites. While the synthetic velocity dispersion shows a similar range in values as the observations, the highest dispersions seen in the observations are associated with regions devoid of ongoing massive star formation. Given the rapid evolution of the central region, it is remarkable that many of the other features are matched.

Comparison between simulations and observations shows that asymmetries in the gas and star formation distribution are a natural outcome of gas flows in galaxies like NGC 1365 (see also Sormani et al. 2018, for the CMZ in the Milky Way), the exact morphology has a transient nature, and there is no need to invoke the impact of an AGN outflow/ionization cone to explain the very efficient formation of many massive star clusters.

5. Toward a Comprehensive Understanding of CMZs

Compared to the CMZ of the Milky Way, the central starburst ring in NGC 1365 is enormous; its extent is $9\times$ larger (while the bar is about twice as long as the Milky Way bar), its SFR is $70\times$ higher, and its dynamical time is about $6\times$ longer. While the inferred molecular gas surface densities and line widths are more comparable to those observed in the Milky Way's CMZ (see Table 1 and Henshaw et al. 2022), they are significantly ($\sim$2–3$\times$) higher than the values typically observed in galactic disks (Sun et al. 2022). At least 37 young ($<$10 Myr), massive ($>10^6 M_\odot$) star clusters are present in the inner 5 kpc region, much more than found in the nearby major merger system Antennae (Whitmore et al. 2023b), and the ring contributes about 30% to the total SFR in NGC 1365.

Our in-depth analysis of the molecular gas and star formation properties of the CMZ in NGC 1365 reveals an inner ($R \leqslant 475$ pc) smooth non-star-forming gas disk similar to those seen in early-type galaxies, a variation in star formation activity along the bar lanes broadly consistent with the pearls-on-a-string scenario (i.e., some location preference for star formation), and no evidence for the AGN impacting the gas disk. This is consistent with Fazeli et al. (2019), who noted tentative evidence for the pearls-on-a-string scenario in the bar lane west of the nucleus based on the analysis of the central $8'' \times 8''$ using near-IR IFU data.

While the dedicated simulation is not meant as a real match of NGC 1365 structures and does not include a practical treatment of radiation or dust, it appears consistent with the main observed gas-related features, which can be explained without invoking AGN feedback. This strongly suggests that the gas morphology and ongoing star formation in the inner 5 kpc of NGC 1365 is caused by the dynamical configuration imposed by the large-scale stellar bar. This is in line with the semiglobal simulations of homogeneous gas inflow by Moon et al. (2021), where the gas inflow rate $\dot{M}_{in}$ controls the SFR in the ring and a close relation of SFR $\approx 0.8 \dot{M}_{in}$ emerges. The follow-up work studying varying gas inflow rates links the variation in SFR mostly to changes in the inflow rate with only a moderate impact by stellar feedback from supernovae and shows that only large asymmetric inflow rates can create a lopsided star formation distribution (Moon et al. 2022). The result of our simulation is also fully consistent with results from simulations of gas flow in a Milky Way–like barred potential of Sormani et al. (2018), which show that the asymmetric and transient gas morphology in the CMZ is induced by large-scale gas flow driven by the bar. These simulations also showed that gas flow in a barred potential is essentially always intrinsically unstable and is bound to develop asymmetric and transient morphologies even in the absence of stellar feedback.

The predicted fast evolution and transient molecular gas pattern for NGC 1365 from the RAMSES simulations can explain the lack of a strong pattern in the age distribution. Note that Seo & Kim (2013) concluded from their simulations that an azimuthal age gradient in star clusters can only develop for low gas inflow rates ($\lesssim 1 M_\odot$ yr^{-1} for their model setup), when the gas entering the ring by switching from the x_1 to the x_2 orbits at the contact points has enough time to collapse and form stars. For higher inflow rates, too much gas enters the x_2 orbits in order to be directly converted into star clusters and thus can continue along the x_2 orbits, leading to a stochastic age distribution. As Elmegreen et al. (2009) estimated a molecular gas mass inflow rate of $\sim$50 $M_\odot$ yr^{-1} (corrected to our assumed

distance but keeping their $4\times$ lower conversion factor from Sakamoto et al. 2007), a stochastic age distribution could be expected.

The lack of a strong pattern in the age distribution is also supported by the simulations of Sormani et al. (2020). These authors compared the instantaneous and time-averaged (over periods of $\sim$20 Myr) distributions of H_2 surface density and the youngest stars in their simulation of the Milky Way's CMZ. They found that the instantaneous gas surface density is clumpy and does not show any evident patterns, while the time-averaged distribution is relatively smooth, with young stars that show a slight preference to form downstream from the apocenter, kind of consistent with the pearls-on-a-string scenario. However, these simulations show that the pearls-on-a-string scenario only becomes evident after taking the time average, and it is very hard, if not impossible, to detect this scenario from a single snapshot that is available for observations.

Based on simulations with and without gas self-gravity and stellar feedback, Tress et al. (2020) concluded that both are required to move gas from the CMZ toward smaller galactocentric radii inside the ring, where it can form a circumnuclear disk. Although their simulations were set up to mimic the situation of the CMZ in the Milky Way, we speculate that the smooth central disk seen in NGC 1365 is fed by similar mechanisms because the RAMSES simulations also include stellar feedback like the simulations of Tress et al. (2020).

The molecular gas morphology in NGC 1365's central 5 kpc is less symmetric than that seen in most other circumnuclear gas rings from barred PHANGS–ALMA galaxies observed at $\sim$1″ (S. Stuber et al. 2022, in preparation). This could imply that other barred galaxies have less variation in the morphology of their central gas reservoir. Clearly, more high-resolution observations are required to build up the necessary statistics to address this question.

6. Summary and Conclusion

By combining $0''\!.3$ (30 pc) resolution PHANGS–JWST MIRI and NIRCAM imaging and archival ALMA CO(2$-$1) mapping with lower angular resolution MUSE data of the central 5 kpc of the nearby barred spiral galaxy NGC 1365, we investigate how star formation proceeds in its wide central starburst ring. The MIRI F770W and F1000W filters reveal the distribution of the neutral gas traced via PAH emission and the location of (embedded) young massive star clusters, respectively, while the ALMA CO data provide access to the molecular gas properties in this region. Together, these data sets provide an unprecedented view of a CMZ undergoing a period of intense star formation. Comparison to hydrodynamical RAMSES simulations of a galaxy with global properties matched to those of NGC 1365 lends insight on the physics underlying the star formation in this distinct structure and CMZs as such. In particular, we find the following.

1. The central molecular gas reservoir is resolved into bright clumpy bar lanes that surround a fainter smooth inner $R_{gal} \sim 5''(\approx 475$ pc) gas disk. This rotating disk is dynamically cold, undergoing circular rotation, and devoid of young massive star clusters. Comparison to stability criteria suggests that this disk is stable against gravitational collapse, similar to what is observed in the

central molecular gas disks of early-type galaxies. As a similar structure develops in simulations via gas inflow caused by stellar supernova feedback (and gas self-gravity), such circumnuclear disks should be a common feature, with actual sizes depending on the exact properties of the large-scale bar and the overall molecular gas reservoir available.

2. The star formation distribution is lopsided. Most young massive star cluster candidates are located along the molecular bar lanes. Some can even be found outside the ring structure, implying that massive clusters are already forming along the bar, i.e., outside the region dominated by x_2 orbits. In the outer southern bar lane, almost no clusters exist, although abundant molecular gas with properties similar to the rest of the bar lanes is present. We speculate that this region is observed just before the onset of star formation.

3. The gas kinematics reveal streaming, i.e., noncircular in-plane, motions and multiple line components in the bar lanes. SCOUSEPY decomposition finds average line widths of $\langle \sigma_{CO,scouse} \rangle \approx 19 \, km \, s^{-1}$ and surface densities of $\langle \Sigma_{H_2,scouse} \rangle \approx 800 M_{\odot} \, pc^{-2}$ that are similar across the central molecular gas structure, implying that the observed high dispersion is caused by intercloud motion between gas peaks. More in-depth analysis in the future has the potential to identify converging flows and relate these to the locations of young clusters.

4. The asymmetric gas distribution observed along the bar lanes is also produced in simulations, where it is transient (changing within a dynamical time) and highly time-dependent in nature. Similarly, the resulting distribution of star formation undergoes rapid evolution in the simulations. This is due to a highly variable gas inflow that stems from the clumpiness of the gas distribution that enters the bar and proceeds to the inner structure. This interpretation is consistent with the 7.7 μm PAH distribution that shows a bright neutral gas disk with a brighter ring superimposed, similar to the time-averaged gas distributions inferred from simulations.

5. There are differences in the overall gas and star formation properties along the gas lanes that are consistent with the time evolution of star formation along the ring. However, the onset of star formation along the gas lanes differs significantly along the two lanes. Based on insights from simulations, this could be linked to asymmetric gas inflow or may emerge from a preference for stars to form downstream from the apocenter of the ring. Also, high gas inflow rates could play a role, as gas entering the ring is not directly converted into stars upon entry but can accumulate along the ring, leading to (some) stochasticity in the star formation.

6. Despite the massive ongoing star formation, the 7.7 μm distribution does not exhibit many bubbles (especially when compared to galactic disks). This might point to the fact that stellar feedback does not significantly alter the gas distribution, though in-depth analysis of the molecular gas kinematics will be required to confirm this.

7. Based on our analysis, we conclude that the massive star formation ongoing in the central 5 kpc of NGC 1365 is driven by gas inflow caused by the large-scale stellar bar and that all star formation–related properties can be explained without invoking any impact of the AGN on the gas disk.

The massive starburst ring in NGC 1365 provides an excellent opportunity to further our understanding of molecular gas accumulation, collapse, and star formation in CMZs. While several of its features appear similar to other star-forming rings observed or seen in simulations, its properties are extreme (especially when compared to the CMZ in the Milky Way). This analysis demonstrates the power of combining high-resolution JWST and ALMA data to gain more insights into the physics controlling the star formation process in CMZs. Studying a sample of nearby CMZs can help to overcome the limitations on our understanding imposed by the time-varying nature of these structures.

Appendix
SCOUSEPY Decomposition

We apply SCOUSEPY (Henshaw et al. 2016, 2019) to the ALMA 0″3 CO(2−1) data cube to decompose the emission lines into individual Gaussian components (Figure 4). For the decomposition, we follow the method applied to the PHANGS–ALMA sample in J. Henshaw et al. (2023, in preparation). We use the "strict_mask" produced by the PHANGS–ALMA pipeline to guide our decomposition (Leroy et al. 2021b), as this mask is tailored to contain high-confidence emission regions. SCOUSEPY divides the spatially masked cube into a Nyquist-sampled set of subregions. We set each subregion to have a width of 35 pixels (i.e., ~1″9) and require that at least 30% of the enclosed pixels are not masked for it to be included in the analysis. This results in 850 subregions covering the masked area. From each of these subregions, a spatially averaged spectrum is extracted and decomposed using derivative spectroscopy (J. Henshaw et al. 2023, in preparation). The parametric description of each parent subregion is then passed as an initial guess for the decomposition of all pixels contained within that subregion. This process depends on a set of tolerance conditions that control the modeling by measuring either the properties of individual components (e.g., their minimum signal-to-noise ratio, which we set to 3, and width, which we set to one channel) or how they compare to the closest matching component in the parent subregion.[41]

To improve the decomposition, we impose the quality control procedure outlined in J. Henshaw et al. (2023, in preparation). Briefly, the quality control process involves two main steps: (i) flagging problematic spectra and (ii) seeking alternative solutions to problematic spectra. Spectra with no associated model solution (typically those that violate the tolerance conditions outlined above), those where the parameter uncertainties are high postdecomposition, or those for which the model solutions differ substantially from those of their surrounding neighbors are flagged. In total, ~28% of the spectra in the masked region were flagged. The vast majority of these flags (~86%) are triggered by spectra with no associated model solution. Broadly speaking, these spectra are located at the edge of the mapped region, where the signal-to-noise ratio is low. The next step is to seek alternative solutions for the flagged spectra. We do this in two ways. First, we attempt to take advantage of the Nyquist sampling of subregions, which can lead to alternative models being available for problematic spectra. Second, where alternatives are not available, SCOUSEPY performs a neighbor-based refit of the spectrum (where we relaxed the condition on the amplitude to also include components of marginal significance, i.e., those with a signal-to-noise ratio >2). After quality control, <7% of the spectra remain flagged, and again, most of them come from pixels where SCOUSEPY was unable to find a suitable solution (top left panel of Figure 4).

ORCID iDs

Eva Schinnerer ⓘ https://orcid.org/0000-0002-3933-7677
Eric Emsellem ⓘ https://orcid.org/0000-0002-6155-7166
Jonathan D. Henshaw ⓘ https://orcid.org/0000-0001-9656-7682
Daizhong Liu ⓘ https://orcid.org/0000-0001-9773-7479
Sharon E. Meidt ⓘ https://orcid.org/0000-0002-6118-4048
Miguel Querejeta ⓘ https://orcid.org/0000-0002-0472-1011
Florent Renaud ⓘ https://orcid.org/0000-0001-5073-2267
Mattia C. Sormani ⓘ https://orcid.org/0000-0001-6113-6241
Jiayi Sun ⓘ https://orcid.org/0000-0003-0378-4667
Oleg V. Egorov ⓘ https://orcid.org/0000-0002-4755-118X
Kirsten L. Larson ⓘ https://orcid.org/0000-0003-3917-6460
Adam K. Leroy ⓘ https://orcid.org/0000-0002-2545-1700
Erik Rosolowsky ⓘ https://orcid.org/0000-0002-5204-2259
Karin M. Sandstrom ⓘ https://orcid.org/0000-0002-4378-8534
T. G. Williams ⓘ https://orcid.org/0000-0002-0012-2142
Ashley. T. Barnes ⓘ https://orcid.org/0000-0003-0410-4504

---

[41] Specifically, the set of tolerance conditions used in this study are tol = [4.0, 3.0, 0.5, 5.0, 5.0, 0.5], and we refer the reader to Henshaw et al. (2016) for further details.

F. Bigiel https://orcid.org/0000-0003-0166-9745
Mélanie Chevance https://orcid.org/0000-0002-5635-5180
Yixian Cao https://orcid.org/0000-0001-5301-1326
Rupali Chandar https://orcid.org/0000-0003-0085-4623
Daniel A. Dale https://orcid.org/0000-0002-5782-9093
Cosima Eibensteiner https://orcid.org/0000-0002-1185-2810
Simon C. O. Glover https://orcid.org/0000-0001-6708-1317
Kathryn Grasha https://orcid.org/0000-0002-3247-5321
Hamid Hassani https://orcid.org/0000-0002-8806-6308
Jaeyeon Kim https://orcid.org/0000-0002-0432-6847
Ralf S. Klessen https://orcid.org/0000-0002-0560-3172
J. M. Diederik Kruijssen https://orcid.org/0000-0002-8804-0212
Eric J. Murphy https://orcid.org/0000-0001-7089-7325
Justus Neumann https://orcid.org/0000-0002-3289-8914
Hsi-An Pan https://orcid.org/0000-0002-1370-6964
Jérôme Pety https://orcid.org/0000-0003-3061-6546
Toshiki Saito https://orcid.org/0000-0001-9016-2641
Sophia K. Stuber https://orcid.org/0000-0002-9333-387X
Robin G. Treß https://orcid.org/0000-0002-9483-7164
Antonio Usero https://orcid.org/0000-0003-1242-505X
Elizabeth J. Watkins https://orcid.org/0000-0002-7365-5791
Bradley C. Whitmore https://orcid.org/0000-0002-3784-7032

References

Agertz, O., & Kravtsov, A. V. 2015, ApJ, 804, 18
Agertz, O., Renaud, F., Feltzing, S., et al. 2021, MNRAS, 503, 5826
Alonso-Herrero, A., Sanchez-Portal, M., Ramos Almeida, C., et al. 2012, MNRAS, 425, 311
Alonso-Herrero, A., Pereira-Santaella, M., Rigopoulou, D., et al. 2020, A&A, 639, A43
Anand, G. S., Rizzi, L., Tully, R. B., et al. 2021a, AJ, 162, 80
Anand, G. S., Lee, J. C., Van Dyk, S. D., et al. 2021b, MNRAS, 501, 3621
Armillotta, L., Krumholz, M. R., DiTeodoro, E. M., & McClure-Griffiths, N. M. 2019, MNRAS, 490, 4401
Astropy Collaboration, Price-Whelan, A. M., Sipőcz, B. M., et al. 2018, AJ, 156, 123
Astropy Collaboration, Robitaille, T. P., Tollerud, E. J., et al. 2013, A&A, 558, A33
Athanassoula, E. 1992, MNRAS, 259, 345
Behrens, E., Mangum, J. G., Holdship, J., et al. 2022, ApJ, 939, 119
Belfiore, F., Santoro, F., Groves, B., et al. 2022, A&A, 659, A26
Bertin, E., & Arnouts, S. 1996, A&AS, 117, 393
Bertoldi, F., & McKee, C. F. 1992, ApJ, 395, 140
Boker, T., Falcon-Barroso, J., Schinnerer, E., Knapen, J. H., & Ryder, S. 2008, AJ, 135, 479
Bolatto, A. D., Wolfire, M., & Leroy, A. K. 2013, ARA&A, 51, 207
Buta, R. J., Sheth, K., Athanassoula, E., et al. 2015, ApJS, 217, 32
Callanan, D., Longmore, S. N., Kruijssen, J. M. D., et al. 2021, MNRAS, 505, 4310
Chevance, M., Kruijssen, J. M. D., Hygate, A. P. S., et al. 2020, MNRAS, 493, 2872
Combes, F., Garcia-Burillo, S., Audibert, A., et al. 2019, A&A, 623, A79
Comeron, S., Salo, H., Laurikainen, E., et al. 2014, A&A, 562, A121
Comrie, A., Wang, K.-S., Hsu, S.-C., et al. 2021, CARTA: The Cube Analysis and Rendering Tool for Astronomy, v2.0.0, Zenodo, doi:10.5281/zenodo.3377984
Davis, T. A., Gensior, J., Bureau, M., et al. 2022, MNRAS, 512, 1522
Edmunds, M. G., Taylor, K., & Turtle, A. J. 1988, MNRAS, 234, 155
Egusa, F., Gao, Y., Morokuma-Matsui, K., Liu, G., & Maeda, F. 2022, ApJ, 935, 64
Eibensteiner, C., Barnes, A. T., Bigiel, F., et al. 2022, A&A, 659, A173
Elmegreen, B. G. 1994, ApJL, 425, L73
Elmegreen, B. G., Galliano, E., & Alloin, D. 2009, ApJ, 703, 1297
Emsellem, E., Monnet, G., & Bacon, R. 1994, A&A, 285, 723
Emsellem, E., Renaud, F., Bournaud, F., et al. 2015, MNRAS, 446, 2468

Emsellem, E., Schinnerer, E., Santoro, F., et al. 2022, A&A, 659, A191
Fazeli, N., Busch, G., Valencia-S, M., et al. 2019, A&A, 622, A128
Forbes, D. A., & Norris, R. P. 1998, MNRAS, 300, 757
Galliano, E., Alloin, D., Pantin, E., et al. 2008, A&A, 492, 3
Galliano, E., Kissler-Patig, M., Alloin, D., & Telles, E. 2012, A&A, 545, A10
Galliano, E., Pantin, E., Alloin, D., & Lagage, P. O. 2005, MNRAS, 363, L1
Galliano, F., Galametz, M., & Jones, A. P. 2018, ARA&A, 56, 673
Gao, Y., Egusa, F., Liu, G., et al. 2021, ApJ, 913, 139
Gensior, J., Kruijssen, J. M. D., & Keller, B. W. 2020, MNRAS, 495, 199
Girichidis, P., Offner, S. S. R., Kritsuk, A. G., et al. 2020, SSRv, 216, 68
Habibi, M., Stolte, A., & Harfst, S. 2014, A&A, 566, A6
Harris, C. R., Millman, K. J., van der Walt, S. J., et al. 2020, Natur, 585, 357
Hassani, H., Rosolowsky, E., Leroy, A. K., et al. 2023, ApJL, 944, L21
Hatchfield, H. P., Sormani, M. C., Tress, R. G., et al. 2021, ApJ, 922, 79
Henshaw, J. D., Barnes, A. T., Battersby, C., et al. 2022, arXiv:2203.11223
Henshaw, J. D., Ginsburg, A., Haworth, T. J., et al. 2019, MNRAS, 485, 2457
Henshaw, J. D., Kruijssen, J. M. D., Longmore, S. N., et al. 2020, NatAs, 4, 1064
Henshaw, J. D., Longmore, S. N., Kruijssen, J. M. D., et al. 2016, MNRAS, 457, 2675
Herrera-Endoqui, M., Diaz-Garcia, S., Laurikainen, E., & Salo, H. 2015, A&A, 582, A86
Hjelm, M., & Lindblad, P. O. 1996, A&A, 305, 727
Hunter, J. D. 2007, CSE, 9, 90
Jones, J., & Jones, B. T. 1980, MNRAS, 191, 685
Jorsater, S., Lindblad, P. O., & Boksenberg, A. 1984, A&A, 140, 288
Kim, J., Chevance, M., Kruijssen, J. M. D., et al. 2021, MNRAS, 504, 487
Kim, J., Chevance, M., Kruijssen, J. M. D., et al. 2022, MNRAS, 516, 3006
Kim, J., Chevance, M., Kruijssen, J. M. D., et al. 2023, ApJL, 944, L20
Knapen, J. H., Shlosman, I., & Peletier, R. F. 2000, ApJ, 529, 93
Kormendy, J., & Kennicutt, R. C. J. 2004, ARA&A, 42, 603
Kristen, H., Jorsater, S., Lindblad, P. O., & Boksenberg, A. 1997, A&A, 328, 483
Krugel, E., & Tutukov, A. V. 1993, A&A, 275, 416
Kruijssen, J. M. D., Longmore, S. N., Elmegreen, B. G., et al. 2014, MNRAS, 440, 3370
Kruijssen, J. M. D., Schruba, A., Chevance, M., et al. 2019, Natur, 569, 519
Krumholz, M. R., Kruijssen, J. M. D., & Crocker, R. M. 2017, MNRAS, 466, 1213
Krumholz, M. R., McKee, C. F., & Tumlinson, J. 2009, ApJ, 699, 850
Lang, P., Meidt, S. E., Rosolowsky, E., et al. 2020, ApJ, 897, 122
Lee, J. C., Sandstrom, K. M., Leroy, A. K., et al. 2023, ApJL, 944, L17
Lee, J. C., Whitmore, B. C., Thilker, D. A., et al. 2022, ApJS, 258, 10
Lena, D., Robinson, A., Storchi-Bergmann, T., et al. 2016, MNRAS, 459, 4485
Leroy, A., Bolatto, A. D., Sandstrom, K., et al. 2023b, ApJL, 944, L10
Leroy, A., Sandstrom, K., Rosolowsky, E., et al. 2023a, ApJL, 944, L10
Leroy, A. K., Schinnerer, E., Hughes, A., et al. 2021a, ApJS, 257, 43
Leroy, A. K., Hughes, A., Liu, D., et al. 2021b, ApJS, 255, 19
Levy, R. C., Bolatto, A. D., Leroy, A. K., et al. 2021, ApJ, 912, 4
Li, G.-X., & Zhang, C.-P. 2020, ApJ, 897, 89
Lindblad, P. A. B., Lindblad, P. O., & Athanassoula, E. 1996, A&A, 313, 65
Lindblad, P. O. 1999, A&ARv, 9, 221
Liu, L., Bureau, M., Blitz, L., et al. 2021, MNRAS, 505, 4048
Liu, D., Schinnerer, E., Cao, Y., et al. 2023, ApJL, 944, L19
Loni, A., Serra, P., Kleiner, D., et al. 2021, A&A, 648, A31
Loose, H. H., Kruegel, E., & Tutukov, A. 1982, A&A, 105, 342
Mandowara, Y., Sormani, M. C., Sobacchi, E., & Klessen, R. S. 2022, MNRAS, 513, 5052
Martin, P. 1995, AJ, 109, 2428
Martín, S., Mangum, J. G., Harada, N., et al. 2021, A&A, 656, A46
McMullin, J. P., Waters, B., Schiebel, D., Young, W., & Golap, K. 2007, in ASP Conf. Ser. 376, Astronomical Data Analysis Software and Systems XVI, ed. R. A. Shaw, F. Hill, & D. J. Bell (San Francisco, CA: ASP), 127
Meidt, S. E., Leroy, A. K., Rosolowsky, E., et al. 2018, ApJ, 854, 100
Moon, S., Kim, W.-T., Kim, C.-G., & Ostriker, E. C. 2021, ApJ, 914, 9
Moon, S., Kim, W.-T., Kim, C.-G., & Ostriker, E. C. 2022, ApJ, 925, 99
Morganti, R., Tsvetanov, Z. I., Gallimore, J., & Allen, M. G. 1999, A&AS, 137, 457
Morokuma-Matsui, K., Bekki, K., Wang, J., et al. 2022, ApJS, 263, 40
Morris, M., & Serabyn, E. 1996, ARA&A, 34, 645
Pan, H.-A., Schinnerer, E., Hughes, A., et al. 2022, ApJ, 927, 9
Querejeta, M., Schinnerer, E., Garcia-Burillo, S., et al. 2016, A&A, 593, A118
Renaud, F., Bournaud, F., Emsellem, E., et al. 2013, MNRAS, 436, 1836
Renaud, F., Romeo, A. B., & Agertz, O. 2021, MNRAS, 508, 352
Rigby, J., Perrin, M., McElwain, M., et al. 2022, arXiv:2207.05632

Robitaille, T., & Bressert, E. 2012, APLpy: Astronomical Plotting Library in Python, Astrophysics Source Code Library, ascl:1208.017
Sakamoto, K., Ho, P. T. P., Mao, R.-Q., Matsushita, S., & Peck, A. B. 2007, ApJ, 654, 782
Sakamoto, K., Okumura, S. K., Ishizuki, S., & Scoville, N. Z. 1999, ApJ, 525, 691
Sandqvist, A., Joersaeter, S., & Lindblad, P. O. 1995, A&A, 295, 585
Sandstrom, K., Koch, E. W., Leroy, A. K., et al. 2023, ApJL, 944, L8
Schinnerer, E., Hughes, A., Leroy, A., et al. 2019, ApJ, 887, 49
Seo, W.-Y., & Kim, W.-T. 2013, ApJ, 769, 100
Seo, W.-Y., Kim, W.-T., Kwak, S., et al. 2019, ApJ, 872, 5
Sheth, K., Vogel, S. N., Regan, M. W., et al. 2002, AJ, 124, 2581
Sheth, K., Vogel, S. N., Regan, M. W., Thornley, M. D., & Teuben, P. J. 2005, ApJ, 632, 217
Sormani, M. C., & Barnes, A. T. 2019, MNRAS, 484, 1213
Sormani, M. C., Binney, J., & Magorrian, J. 2015, MNRAS, 449, 2421
Sormani, M. C., Tress, R. G., Glover, S. C. O., et al. 2020, MNRAS, 497, 5024
Sormani, M. C., Treß, R. G., Ridley, M., et al. 2018, MNRAS, 475, 2383
Spoon, H. W. W., Marshall, J. A., Houck, J. R., et al. 2007, ApJL, 654, L49
Stark, A. A., Martin, C. L., Walsh, W. M., et al. 2004, ApJL, 614, L41
Stevens, I. R., Forbes, D. A., & Norris, R. P. 1999, MNRAS, 306, 479
Storchi-Bergmann, T., & Bonatto, C. J. 1991, MNRAS, 250, 138
Sun, J., Leroy, A. K., Rosolowsky, E., et al. 2022, AJ, 164, 43
Tan, J. C. 2000, ApJ, 536, 173
Teng, Y.-H., Sandstrom, K. M., Sun, J., et al. 2022, ApJ, 925, 72
Teyssier, R. 2002, A&A, 385, 337
Toomre, A. 1964, ApJ, 139, 1217
Tress, R. G., Sormani, M. C., Glover, S. C. O., et al. 2020, MNRAS, 499, 4455
Turk, M. J., Smith, B. D., Oishi, J. S., et al. 2011, ApJS, 192, 9
Turner, J. A., Dale, D. A., Lee, J. C., et al. 2021, MNRAS, 502, 1366
van den Bosch, R. C. E. 2016, ApJ, 831, 134
Veilleux, S., Maiolino, R., Bolatto, A. D., & Aalto, S. 2020, A&ARv, 28, 2
Veilleux, S., Shopbell, P. L., Rupke, D. S., Bland-Hawthorn, J., & Cecil, G. 2003, AJ, 126, 2185
Venturi, G., Nardini, E., Marconi, A., et al. 2018, A&A, 619, A74
Ward, J. L., Kruijssen, J. M. D., Chevance, M., Kim, J., & Longmore, S. N. 2022, MNRAS, 516, 4025
Watkins, E. J., Barnes, A., Henny, K. F., et al. 2023, ApJL, 944, L24
Whitmore, B., Chandar, R., Lee, J. C., et al. 2023a, MNRAS, in press
Whitmore, B., Chandar, R., Rodríguez, M. J., et al. 2023b, ApJL, 944, L14